Set-up, South Pole field test and energy threshold determination of the Erlangen design of an IceAct telescope.

Master's Thesis in Physics

presented by

Stefan Dietz

July 18, 2019

Erlangen Centre for Astroparticle Physics
Friedrich-Alexander-Universität Erlangen-Nürnberg

Supervisor: **Prof. Dr. Stefan Funk**
Co-Advisor: **Dr. Adrian Zink**

Abstract

The IceAct telescope is a Cherenkov Telescope initially developed and named after its main application - to veto terrestrial neutrinos for IceCube. The Fresnel lense based design, differentiating it from the more common mirror based designs, allows for some outstanding properties. The whole telescope weighs just ~ 20 *kg and runs on just 36 W power. It also features a large field of view of 12.6* ^{o} *distributed on 64 SiPM pixels with 1.2* ^{o} *each. The low number of SiPMs allows for outstanding manufacturing costs of less than 10k€ per telescope. This includes the TARGET C/T5TEA based readout electronics and makes IceACT economical for large array applications.*

Based on the work of Kristof Kremer, who tested a single SiPM connected to a single readout channel, the full camera with all 64 pixels was set up, tested and improved during this thesis. Winston cones from different fabricants were examined and compared. A calibration of the camera was performed by measuring under homogeneous illumination. The resulting correct for intrinsic differences in arrival time and intensity between the different pixels.

Software to control the telescope based on the TARGET Software was developed. This includes a function that keeps the gain constant to achieve even better data homogeneity. A low-level analysis based on gaussian fits was evolved, which was sufficient for the measurements within this thesis. A real reconstruction of the shower properties based on the IceAct shower images, however, will be one of futures most urgent tasks.

The whole telescope was successfully tested down to $-50^o C$ *outside temperature in a cooling chamber at RWTH Aachen. IceActs were deployed at Erlangen, Namibia and the South Pole. Despite the strongly varying climate, IceAct worked reliable at all three sites, producing clear shower images. For each measurement the total size spectrum follows a power law as expected for the cosmic ray flux.*

Due to the absence of a reconstruction of the IceAct images, it was necessary to measure in coincidence with the H.E.S.S. array in Namibia to obtain an energy spectrum of IceAct. With it, its energy threshold - a property of major importance, in particular for the veto application - could be determined to ~ 11 *TeV.*

Contents

1 Introduction

The attention to the sky and its riddles was born with the human species itsself. From bone sticks with markings indicating the awareness of the lunar phases dating back to 35000 BC over celtic stone circles proofing well understanding of the annual movement of the sun to the first image of the night sky from the bronze age, the Nebra sky disk (1600 BC) - ever since humans left their traces, they showed affection to the sky and its secrets. [30]
Clay tablets with records of celestial bodies by the Sumerians date back to 3200 BC. [17] Their studies in early Mesopotamia, like dividing a circle into 360 degrees with 60 minutes each, laid the foundations to astronomy in the Hellenistic world, which can arguably count as the time of birth of astronomy as a natural science and makes it the oldest among all.
The Greeks were limited to observation by naked eye. Since then, however, technological progress empowered us to observe more and more previously unknown sources and messengers, which had great impact on our society and self conception.
In 1609 Galileo Galilei used the first optical telescope to observe fainter sources of visible light and already known ones in greater detail. His studies lead to the transition to the heliocentric system, contradicting one of the most commonly held believes at that time.
The next great step followed as one was able to observe the full electromagnetic spectrum and perform spectral analysis. Erwin Hubble measured the redshift of other galaxies and concluded an expansion of the universe. [25] In reverse, in 1929 he evolved the theory of a big bang, giving an answer to one of the most frequently asked question throughout millenia and cultures - the origin of the universe. In 1964 Arno Penzias and Robert W. Wilson strongly supported this theory by detecting the Cosmic Microwave Background. [37]
Cosmic rays were added to the observable messengers in the early 20th century, leading to great progress in high energy and particle physics, such as better understanding of supernovae, the early universe or the Standard Model of Particles.
Not by chance it took until 1968 for Ray Davies being the first to detect extraterrestrial neutrinos. [18] The absence of a charge as their very low mass result in very low probabilities for interactions with other particles. Although this makes them difficult to detect, it also makes them superior to other messengers. While charged cosmic rays loose their directional information by interaction with the various electromagnetic fields present in the universe, neutrinos are assumed to originate in the direction they are coming from. Charge- and massless photons also keep their direction, however, they can be absorbed by matter, such as the intergalactic dust. On the other hand, it is difficult to measure neutrinos with high significance due to their extremely low cross sections.
This thesis contributes to improve the statistics of IceCube, a large neutrino observatory

at the South Pole. It is designed to detect extraterrestrial neutrinos, however, IceCube can not well distinguish those from neutrinos created in air showers from cosmic rays within the earth's atmosphere. An array of IceACT telescopes will detect such air showers and in case of a time coincidence with an IceCube event, latter is assumed to be a terrestrial neutrino and vetoed.
One major goal is observing neutrino point sources, which will give us a key to the early stages of the most energetic processes in our universe. While all other messengers are highly effected by the later stages of the process, neutrinos escape at any time, providing previously unknown information. This would allow us a deeper look into the fundamental physical processes or even get closer to the very origin of our universe itself. By that, neutrino astronomy yields the potential of heralding another era of great progress in our deep desire to understand the universe we exist in.

1.1 Cosmic radiation

Cosmic rays (CR) are high energy particles from extraterrestrial sources first detected by V. Hess in 1912. [24] CR energies range from $\sim 10^7$eV up to the highest ever measured particle with an energy of $3 \cdot 10^{20}$eV [10], as can be obtained from their energy spectrum shown in Fig. 1.1. While mainly decreasing with a power law of the exponent of -2.7, two features can be observed: a steepening of the spectrum ("knee") at energies $\sim 10^{15}$ eV and a hardening ("ankle") at $\sim 10^{18}$ eV.
Some types of supernova remnants are expected to accelerate particles up to energies of $\sim 10^{15}$ eV. Assuming that the CR spectrum up to the "ankle" is dominated by sources within our galaxy and these supernove types make up for a significant amount of particle accelerators in our galaxy, the "knee" could be explained by this cut-off energy. [6]
KASKADE measurements revealed a difference of the position of the knee in the γ-ray and the heavy nuclei spectra, which could be related to the charge of the particle. The presence of magnetic fields in the vicinity of the accelerators, which act more efficiently on the higher charged particles, could as well contribute or even account for the existence of the "knee". [21]
On larger scale, the galactic magnetic field confines charged particles within our galaxy, however, they can escape as their energy is sufficient. From KASKADE-Grande measurement it was possible to determine this escape energy to $\sim 10^{17}$ eV. It follows that the CR spectrum above the "ankle" is dominated by extragalactical particles. [21] Since charged particles loose their directional information in the various electro-magnetic fields present in the universe, it is difficult to determine their sources. Good candidates are active galactic nuclei (AGNs), but reliable studies are difficult due to the low statistics. However, neutrinos could also be the key in this search. Low statistics are also the reason why it is still unclear if the few measured particles above the GZK cut-off energy of $\sim$ 3-5 $\cdot 10^{19}$ eV contradict the popular theory of high energy proton interactions with the photons of the Cosmic Microwave Background (CMB).
The composition of the cosmic radiation remains more or less constant over the whole

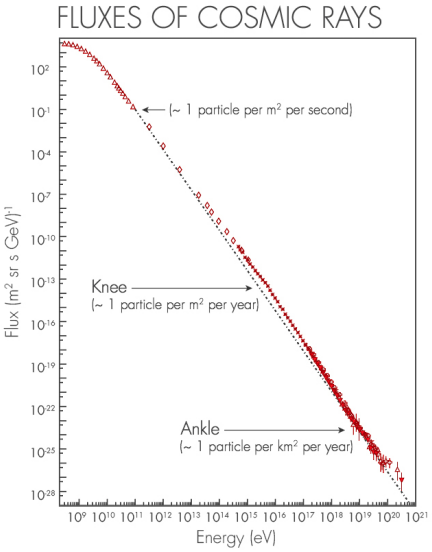

Figure 1.1: **Cosmic ray energy spectrum.** The CR energy spectrum (red data points) covers ∼14 orders of magnitude. It mainly decreases with a power law with an exponent of -2.7 (black line) with just small deviations at the "knee" at $\sim 10^{15}$ eV and the "ankle" at $\sim 10^{19}$ eV. Their origin is still part of intense studies, but the most popular theories indicate that the "knee" is a result of different intragalactical processes and the ankle marks the point where extragalactical CRs begin to dominate the spectrum. [38]

energy spectrum. [6] Protons ($\approx 87\%$) and α-particles ($\approx 12\%$) are the dominant parts of their charged component and the remaining consists of heavier, fully ionized nuclei or electrons. [12, 29] Depending on the definition of cosmic rays, one can add a much smaller fraction of uncharged particles like high energy photons (γ-rays) or neutrinos. Cosmic rays can be detected directly by satellites in space, however, the fluxes drop very fast with increasing energy. Larger detector volumes are needed to compensate for this effect and still gain sufficient statistics on reasonable time scales. This limits direct CR detection by satellites in space up to energies of ~ 300 GeV. [29] To detect higher energy CRs, ground-based detectors observing the earth's atmosphere are used. They no longer detect the primary cosmic ray particle, but the Cherenkov-light emitted by the secondary particles created by interaction with the gas molecules.

1.2 Particle air showers

Cosmic rays with enormous energies hit the earth's atmosphere. In presence of the gas molecules, which can account for momentum conservation, they decay into secondary particles. The created particles still have great energies and decay on their own, creating a cascade of secondary particles named a particle shower. The more particles are

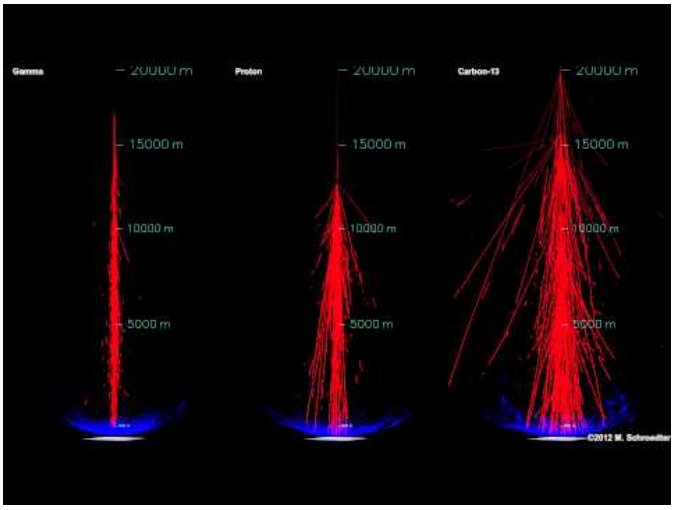

Figure 1.2: **Simulation of air showers of different incident particles.** Secondary particle structure (red lines) and resulting Cherenkov cone (blue) for an electromagnetic shower (left) and hadronic showers from an incident proton (middle) and a carbon nucleus (right). [34]

created, the less energy remains for each of them. The shower maximum is reached, as the new created secondary particles become less than those lost through collisions with air molecules. As the average energy per particle drops below a critical energy, where no more secondary particles can be produced, the shower dies out.

1.2.1 Shower Types

Electromagnetic showers are induced by incident γ-rays. As the incident photon hits the atmosphere, an electron-positron pair (e^-e^+-pair) is created and its energy is distributed on them. This so called pair production is one fundamental processes, that create secondary particles in an electromagnetic shower. "Bremsstrahlung", the other, is the emission of photons by fast (secondary) e^- or e^+. Due to the low mass of the $e^{-/+}$ the major part of their energy is of kinetic nature, which is the cause for the slim structure of electromagnetic showers (Fig. 1.2 left).
In the case of hadronic showers the incident proton/nucleus interacts with an air molecule and creates secondary hadrons, charged (π^+,π^-) and uncharged (π^0) pions. The π^0 decays after a mean lifetime of $(8.4 \pm 0.4) \cdot 10^{-17}$ s into two γ-rays, which cause electromagnetic subshowers. The hadrons and charged pions interact again, creating new secondary particles. Similar to the electromagnetic case this continues until a critical energy is reached and no more pions can be produced. The remaining $\pi^{+/-}$ decay into $\mu^{+/-}$ and $\nu_\mu/\bar{\nu_\mu}$. The higher masses of hadrons and pions compared to electrons as well as the higher number of kinds of secondary particles cause the more wide-spread angular dependence of the secondary particles in hadronic showers. The higher the mass of the

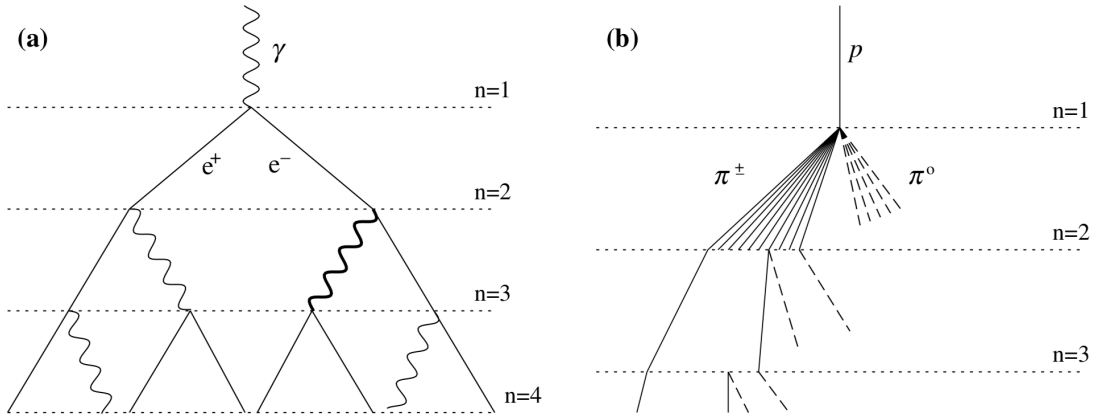

Figure 1.3: **Heitler schematics of showers.** Schematic view of electromagnetic (a) and hadronic (b) showers. The hadronic model spares the electromagnetic subshowers from the π^0-dacay (dashed lines) and secondary nuclei. For both models n indicates multible splitting lengths, which is the distance between interactions in the medium. [31]

incident nucleus, the stronger is this effect (Fig. 1.2 middle and right). [31]

1.2.2 Shower characterization with Heitler model

Depending on the energy of the incident particle, up to an order of $\sim 10^{10}$ charged secondary particles can occur in CR air showers. Computational power allows for good numerical simulations, yet simple models are sufficient to accurately predict the most relevant properties of air showers. Bethe and Heitler developed such a model for electromagnetic showers in 1954 [22], which was later transferred on hadronic showers by Matthews [31].

Electromagnetic Showers

Bethe and Heitler assumed that secondary particles within electromagnetic showers are only created by single photon bremsstrahlung ($e^{+/-} \rightarrow e^{+/-} + \gamma$) or pair production ($\gamma \rightarrow e^+ + e^-$). They furthermore assumed, that the radiation length λ_r for both processes is equal. With that they could define the distance a particle travels before decaying to two secondary particles as splitting length

$$d_e = \lambda_r \cdot \ln(2)\,. \tag{1.1}$$

From that follows the total number of particles in the shower

$$N(x) = 2^n = 2^{\frac{x}{d_e}} \tag{1.2}$$

depending on the distance x to the first impact point in multiples n of the splitting length d_e.
With another simplification, that independent of the process the energy is equally devided between the created particles, the energy per particle after n splittings is

$$E(n) = \frac{E_0}{2^n} \tag{1.3}$$

where E_0 is the energy of the primary cosmic ray. Note that energy losses due to ionization of air molecules are neglected as well.
Heitler defines a critical energy E_c^e, below that no longer secondary particles can be created by bremsstrahlung or pair production and the $e^{+/-}$ loose their remaining energy by ionizing air molecules on the way. It depends on the medium and for air $E_c^e = 85$ MeV. Consequently after $n_{\max}$ splitting lengths the maximal number of shower particles

$$2^{n_{\max}} = N_{\max} = \frac{E_0}{E_c^e} \tag{1.4}$$

is reached, where

$$n_{\max} = \frac{\ln\left(\frac{E_0}{E_c^e}\right)}{\ln(2)}. \tag{1.5}$$

Inserting $n_{\max}$ in equation 1.1 yields the penetration depth

$$X_{\max}^e = \lambda_r \cdot \ln\left(\frac{E_0}{E_c^e}\right) \tag{1.6}$$

of the shower in the medium.
Detailed simulations and experiments confirm the proportionality of the shower size and the logarithmic dependence of the penetration depth of E_0. Even the calculated quantitative numbers are in the right order of magnitude, however, the number of electrons in the shower

$$N_e = \frac{N}{g} \tag{1.7}$$

is overestimated and can be corrected for by a constant factor $g = 10$. A schematic of an electromagnetic shower under the assumptions of the Heitler model is displayed in Fig. 1.3 (a).

Hadronic showers

Matthews tries to expand Bethe and Heitlers model on more complex hadronic showers. His approach is to find parameters according to Bethe and Heitler for hadronic interactions in a particle shower induced by a proton. Instead of a radiation length a interaction length $\lambda_I \approx 120$ g/cm^{-2} is defined, which can be assumed constant for pions

in the energy range from 10-1000 GeV, where most interactions in showers with incident energies around the "knee" happen. After a distance

$$d_p = \lambda_I \cdot \ln(2) \tag{1.8}$$

the hadrons interact, creating N_{ch} charged and $\frac{1}{2}N_{ch}$ uncharged pions. For an energy range of 1 GeV - 10 TeV it can be approximated as constant with $N_{ch} = 10$. In the hadronic case, the critical energy E_c^p is defined as the energy where the decay length becomes less than d_p. It decreases with increasing E_0, but will be assumed constantly equal to 20 GeV.
After n interactions the average energy of the charged pions is

$$E_\pi = \frac{E_0}{\left(\frac{3}{2}N_{ch}\right)^n} \tag{1.9}$$

with the missing part in the electromagnetic sub-showers from the π^0-decay. It follows for the critical interaction number

$$n_{max} = \frac{\ln\left(\frac{E_0}{E_c^p}\right)}{\ln\left(\frac{3}{2}N_{ch}\right)}. \tag{1.10}$$

The primary energy of the proton

$$E_0 = E_c^e \cdot N_{\max} + E_c^p \cdot N_\mu \tag{1.11}$$

is distributed over the electromagnetic sub-showers as well as the muons from decaying charged pions, where $N_\mu = N_{ch}$. With equation 1.7 and the approximated parameters including $\lambda_r = 37\mathrm{g/cm}^{-2}$ follows for the reconstruction of the incident energy

$$E_0 = gE_c^e\left(N_e + \frac{E_c^p}{gE_c^e}N_\mu\right) \approx 0.85\mathrm{GeV}\,(N_e + 24N_\mu) \tag{1.12}$$

in dependence of the number of electrons and muons reaching the ground.
Assuming the electromagnetic sub-showers dominate the particle number and just taking into account the first interaction at $n = 1$, the penetration depth of the hadronic shower can roughly be approximated by an electromagnetic shower with the energy $\frac{E_0}{3N_{ch}}$. This fraction of E_0 remains, since just one third of the incident energy goes into the N_{ch} photons created by the $\frac{1}{2}N_{ch}$ uncharged pions, that induce parallel developing sub-showers. With equation 1.6 and the first interaction taking place at $X_0 = \lambda_I \ln(2)$ follows the penetration depth of hadronic showers

$$X_{\max}^p = X_0 + \lambda_r \ln\left(\frac{E_0}{3N_{ch}E_c^e}\right). \tag{1.13}$$

Fig. 1.3 (b) shows a schematic picture of a hadronic shower under the assumptions of Matthews.

Typical shower around the cosmic "knee"

The Heitler models are a good starting point to predict the basic properties of air showers. Moreover they shed light on the underlying fundamental physical processes of shower development, however, for a detailed analysis numerical models remain essential.
Since the majority of CRs are protons and the IceAct telescope is most efficient for energies $\sim$ 100 TeV, a hadronic shower with an incident energy of 10^{14} eV serves as a typical example for a shower here. Under the (rather rough) assumption of a constant air density $\rho_{\text{air}} = 0.74 \cdot 10^{-3}\ \frac{\text{g}}{\text{cm}^3}$, which is the value for a height of 5 km above sea level [14], from equation 1.13 with all the parameters used above the shower depth

$$\frac{X^p_{\text{max}}}{\rho_{\text{air}}} \approx 6,4\text{km} \tag{1.14}$$

can be determined.
Even the secondary particles are highly relativistic and the shower development speed assumed to be $\sim c$. This leads to shower evolution times on the order of $\sim$ 20 ns.
For typical first impact points $\sim$ 10 km above sea level [13], typical shower maxima occur at heights $h \approx 3.6$ km above sea level for hadronic showers with energies around the "knee". Note again that this is a rough approximation, not least since the air density strongly varies with altitude.

1.3 Cherenkov radiation

Cherenkov radiation, named after the soviet nobel prize winner of 1958 Pavel Alekseyevich Cherenkov, is emitted if a charged particle travels faster than the phase velocity of light inside a dielectric medium. [27] In a classical picture the charged particle disturbes the local fields and polarizes the dielectric medium at its current position. In most cases this polarization relaxes back to normal as the particle travels on. However, if the particle speed exceeds the speed of the relaxation, a part of its energy will beand the particle left in a trace of polarization along its path and radiated by coherent emission of photons. [26]
The speed of light in vacuum c is an universal constant, however, in medium it is reduced by the reciprocal refractive index giving

$$c' = \frac{c}{n}. \tag{1.15}$$

Fig. 1.4 shows the geometry of the emission. The Cherenkov photons travel at less speed than the particle and consequentely in the reference frame of the particle only backward emission is allowed. This leads to a cone-like emission of photons with the particle at the front, which is phenomenologically equal to the more commonly known effect of the supersonic cone. [27] In a time interval t, the shock front travels the distance $d_s = \frac{c}{n}t$ while the particle travels $d_p = \beta ct$. From that follows the equation

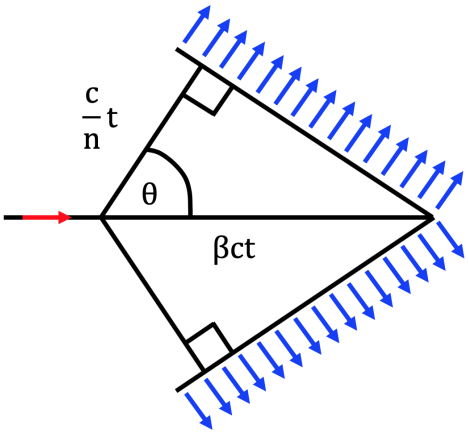

Figure 1.4: **Geometry of Cherenkov cone.** The charged particle travels in the direction of the red arrow with the speed βc, while the emitted Cherenkov photons just travel at the speed of light in medium $\frac{c}{n}$. The distances travelled in a time t by the particle βct as well as the Cherenkov photons $\frac{c}{n}t$ determine the opening angle of the cone by $\cos(\theta) = \frac{1}{n\beta}$. [26]

$$\cos(\theta) = \frac{d_s}{d_p} = \frac{1}{\beta n} \tag{1.16}$$

for the opening angle θ, which can only be satisfied for $\beta \geq \frac{1}{n}$.
Cosmic rays are accelerated to such enormous energies, that even a large number of secondary particles exceed the speed of light in air, so they are assumed to be highly relativistic and $\beta \approx 1$. Together with equation 1.16 one can give the opening angle

$$\theta = \cos^{-1}\left(\frac{1}{n}\right) \tag{1.17}$$

just depending on the refraction index n. The refraction index of air grows with lower altitudes, which leads to greater opening angles, as Fig. 1.5 illustrates. However, cones emitted closer to the ground have less time to spread, and this is the reason why they roughly cover similar areas as those created higher in the atmosphere. [9]
The intensity of the Cherenkov radiation I_C emitted by an air shower is proportional to the amount of created secondary particles, which is itself proportional to the incident energy of the CR, so

$$I_C \sim E_0. \tag{1.18}$$

Frank and Tamm found, that the spectrum of Cherekov radiation is continuous and favors smaller waveleghts. [19] Thus the majority of the Cherenkov light from CR air showers is in the ultraviolet range.
The required minimal energy of a particle to emit Cherenkov light

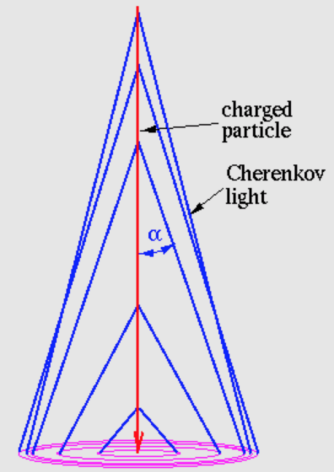

Figure 1.5: **Cherenkov light from Air Shower.** The initial charged particle travels along the shower axis in the direction of the red arrow. Every secondary particle emits a cone with increasing opening angle due to the rising n of air with lower altitudes. Depending on incident energy, angle and particle species, a unique conic section can be observed at the ground.[9]

$$E_{\text{min}} = \gamma \cdot m_0 \cdot c^2 \tag{1.19}$$

is proportional to the rest mass m_0 of the particle. It follows, that the major part of the Cherenkov emission of an air shower arises from the lighter particles (e. g. $e^{+/-}$). Incident γ-rays produce just one Cherenkov flash, while the electromagnetic subshowers in hadronic events induce a more ragged pattern, giving one possibility to distinguish between them. [29]

1.4 IceACT

The IceAct telescope is an Imaging Atmospheric Cherenkov Telescope (IACT), designed to detect the Cherenkov flashes created by air showers. As mentioned, the rapidly falling fluxes with rising energy in the CR spectrum limits direct detection by satellites and above $\sim$ 10 TeV ground based IACTs take over. Their effective area is much larger compared to satellites, since they use the atmosphere as target volume.
The Cherenkov flashes produced by the air showers are rather faint, in particular compared to the various amount of terrestrial and extraterrestrial light sources called the night sky background (NSB). So the photons from the atmosphere get collected, either by mirrors or lenses, and focused on a camera consistent of silicon photo multipliers (SiPMs). Without filters, which increase cost and size of the structure, these can not distinguish between different wavelengths and such it is not economically to use spectral features to distinguish between Cherenkov and NSB photons. However, the flow of NSB

	HESS II	MAGIC	CTA (small)	IceACT
location	Namibia	La Palma	La Palma/Chile	South Pole
field of view	3.2 °	3.5 °	8.8 °	12 °
collection area	614 m^2	236 m^2	7.5 m^2	0.3 m^2
energy range	10GeV-10TeV	25GeV-30TeV	5-300TeV	$\sim$ 100 TeV
weight	580 tons	60 tons	8.6 tons	20 kg
power consumption	8 kW	-	-	36 W

Table 1.1: **Properties of selected IACTs.** Basic properties of the IACTs built for HESS II [3] and MAGIC [4] as well as the planned small telescope for CTA [1] in comparison with the IceACT telescope.

photons is continuous while the Cherenkov light flashes on the order of $\sim$ 10 ns (section 1.3). In these short time scales NSB photons are few (at least for clear skies with not too much artificial light) compared to the blast-like emitted Cherenkov photons.
Very fast camera electronics with $\sim$1 Gigasample per second are needed to resolve the short flashes (more detail in section 2). To avoid the collection of excessive amounts of data a trigger is used. From cut criteria, like the amount of photons measured within a short time interval or the geometric distribution throughout the camera, a boolean signal is created. In the case it gives high, it is assumed that a Cherenkov event took place and a time window well large enough to record the full SiPM peak ($\sim$ 100 ns) of the sampled data is digitized.
Arrays of IACTs in joint operation improve the intrinsic properties of the single telescopes. Together they cover a larger fraction of the atmosphere from which a larger field of view follows. They also observe the same shower from different angles, which greatly improves the reconstruction of shower parameters like the incident energy, the first impact point and the particle species. Currently operating IACT arrays are e. g. High Energy Stereoscopic System (H.E.S.S.) or Major Atmospheric Gamma Imaging Cherenkov Telescopes (MAGIC). The design for the Cherenkov Telescope Array (CTA) is currently in the making, as it is for IceACT.

1.4.1 Telescope Properties

The IceACTs primary application is a planned extension of the IceTOP array at the South Pole. In contrast to H.E.S.S. or MAGIC its main goal is a coverage of the sky as large as possible at reasonable costs.
Even though the single IceACT telescopes will feature a large field of view of $\sim 12°$ compared to other IACTs, to achieve a full sky coverage at one site an array of 253 telescopes is required (Fig. 1.6 (a)). To keep overall costs reasonable, this number limits the budget for the single telescopes. At predicted costs per telesope of < 10k€ a comparably simple structure (section 2) was chosen. The light is collected by a Fresnel lens with a diameter of $\sim$ 60 cm, which leads to a small collection area of just $\sim$ 0.3 m^2. However,

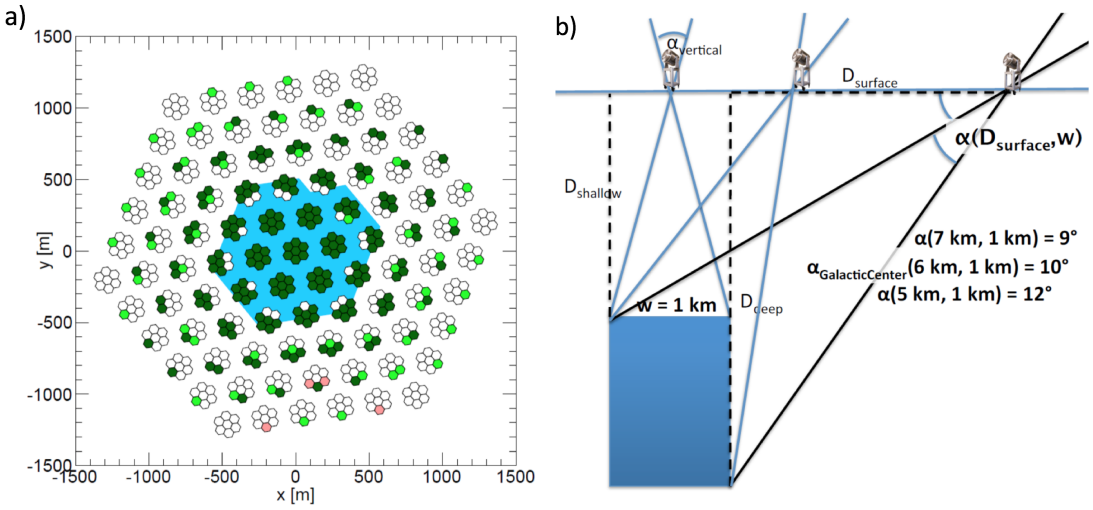

Figure 1.6: **Possible South Pole Array designs.** (a) Array with roughly the same opening angle as IceTOP but a lower threshold (50 GeV instead of 300 GeV). Blue area indicates the area of the existing IceTop array. Seven hexagons indicate groups of IceACT telescopes with different viewing directions with a combined field of view of 18°. The colors indicate importance (dark green being most important) and the white ones are not needed. [8] (b) Geometry of a veto array including the Galactic Center region. Solid lines indicate potential particle trajectories through IceCube and give requirements for the field of view. The inner part of the array is similar to the inner part of a) with an additional ring of $\sim$ 30 telescopes at a distance of $\sim$ 6 km of the IceCube center (blue rectangle). [7]

the small design comes with a low weight of $\sim$ 20 kg which ensures good move-ability. On top, the usage of the lens instead of mirrors allows for a compact design, which is more sustainable in extreme conditions such as in the polar night.
The camera features 64 SiPMs consuming together with the TARGET Readout Electronics just $\sim$ 36 W, which proofs to be a another great advantage, for power generation is expensive at remote locations such as the South Pole.

1.4.2 The South Pole Array

The main (and naming) application of the IceACT is the planned array at the geographic South Pole. It is intended to be located right above the IceCube observatory.
IceCube is an underground neutrino detector, located 1.45 km below the surface. 5160 photomultipliers distributed along 86 strings build a three dimensional grid on a volume of one cubic kilometre of Antarctic ice. As a neutrino interacts in it, secondary particles are created. These emit Cherenkov radiation eventually revealing the origin and initial energy of the neutrino.
IceCube is interested in extraterrestrial neutrinos, but can not well distinguish them from terrestrial secondary neutrinos created in CR air showers. One intrinsic option to do so is the incident direction of the neutrino. If it has crossed the earth and entered the detector from below, it is believed to be extraterrestrial since the flow of secondary neutrinos in far distance of the shower is low compared to the constant extraterrestrial component. However, it is different for neutrinos entering from above. A surface array of 162 ice tanks, IceTop, was added to the detector to measure secondary particles of air showers. If such an event occurred in coincidence with a neutrino event in IceCube, this event is vetoed. IceTop, however, just covers a field of view of 37° vertically above IceCube, leaving a large part of the nightsky unchecked - in particular the interesting region of the Galactic Center at a declination of 29°. [8]
As mentioned, IceACT allows for large, economically justifiable arrays. Fig. 1.6 (a) shows the design of a veto array of 253 telescopes with a field of view of $\sim$ 18°. With a predicted threshold of $\sim$ 50 TeV, the IceACT South Pole array it is a factor of 6 below the one of IceTop. This difference would significately increasing the statistics on pure astrophysical events detected by IceCube. [8] Another proposed design features just the inner part and a ring of $\sim$ 30 telescopes in a distance of 6 km of the IceCube center (Fig. 1.6 (b)). It is on the same order of needed telescopes but would cover a region of $\sim$ 2° around the galactic center. [7]
An array of $\sim$ 7 IceAct telescopes is sufficient to determine the kind of nucleus of the incident CR with reasonable precision. [16] Although it is believed that the composition does not underly major changes for different energies, already tiny variations could help to determine the origin of the CRs and shed light on the processes that accelerated them. [6] One region of major interest is the "knee" at $\sim$ 1 PeV in the CR spectrum. Showers of CRs at of this energy range have shower maxima at $\sim$ 3.6 km altitude (section 1.2) giving a detector at $\sim$ 2.8 km (altitude of the South Pole) a front row seat to observe them. [16]

2 Components

Fig. 2.1 shows the components of the IceAct telescope. A Fresnel lens embedded in a plastic mounting ring is covered by a glass plate. To avoid moisture on the cold glass, it is heated some degree above outside temperature by a heating cable inside the plastic ring, evaporating all moisture in the dry environment. All that sits on top of a carbon fibre glass tubus, which was later replaced by a even cheaper and less heavy plastic version. The bottom of the tubus is closed and shielded to stray-light by another plastic plate. It features a circular hole for the upwards pointing camera and holds a solid box of aluminium that contains the electronics for control and readout. Two heating circles bring, if not already achieved by regular power consumption, the box inside to operational temperatures of the readout electronics.
With a total weight of less than 20 kg the whole telescope is still light enough to be mounted on a standard telescope mount allowing for free move-ability and active tracking.

2.1 Light collection

Large SiPMs have higher effective areas, however, they are by far more expensive. Even the small SiPMs used for this telescope make up for $\sim 50\%$ of the total cost. On the other hand they are superior to large SiPMs in terms of image quality. To counter the deficit in effective area, the incident light is collected and focused on them.

2.1.1 Fresnel lens

Instead of mirrors, a Fresnel lens of a diameter of ~ 60 cm is used. It is thinner than conventional lenses and therefore absorption of UV light in the lens material is minimized. This comes at the cost of less image quality, however, it is still sufficient for this camera type with 61 pixels with an opening angle of 1.2° each. To minimize scattering losses, the lens is protected from scratches by a layer of silica fused glass located right above. On a focal length of ~ 502.1 mm, which is the height of the tubus, the lens focuses the photons on a position on the camera plate (diameter of ~ 14 cm) depending on the incident angle (Fig. 2.2).

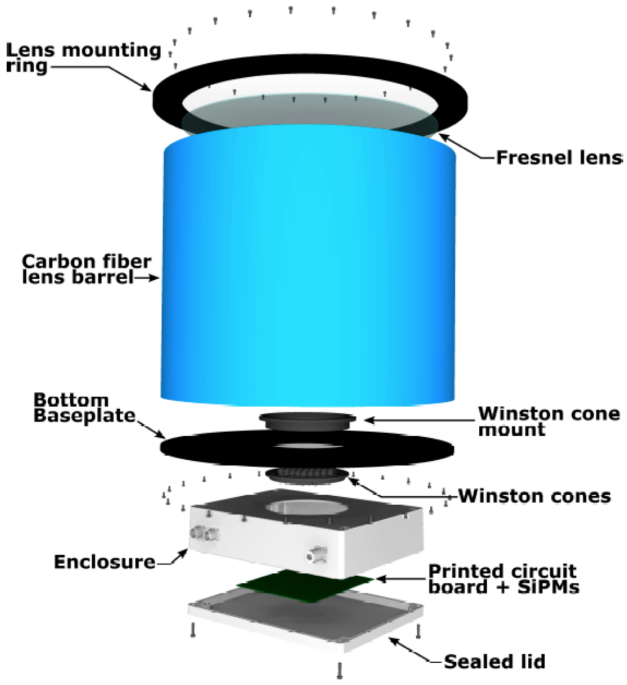

Figure 2.1: **Components of the telescope.** A Fresnel lense of ~ 60 cm diameter sits on top of a carbon fiber glass tubus. It boundles the light along the tubus height of ~ 60 cm on the camera holding the SiPMs with the Winston cones. The readout electronics are located right below the camera and are protected from environmental influences by an enclosure of solid aluminium. [29]

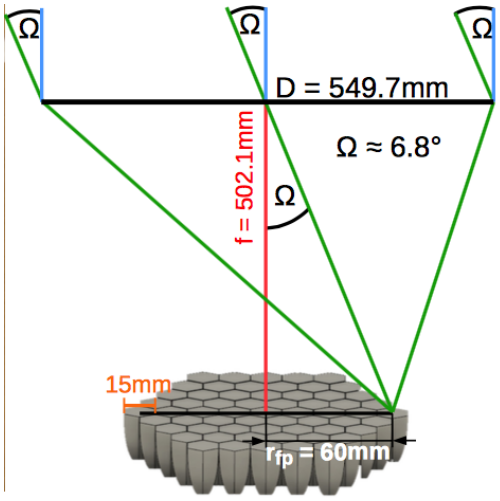

Figure 2.2: **Light collection by the Fresnel lense.** Depending on the incident angle $-6.8° < \Omega < +6.8°$, the photons get focused on a distinct position on the camera plane. [28]

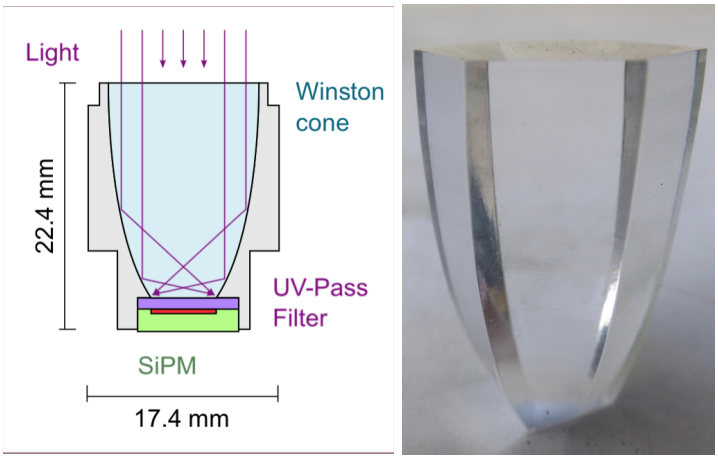

Figure 2.3: **Schema [33] and Close-up photo of a Winston cone.** All photons entering the hexagonal top surface will leave the cone through the square bottom surface and are directly sent into the SiPM. This increases the effective area of the SiPMs by the fraction of these surfaces, in this case ∼5.85.

2.1.2 Winston cones

The SiPMs just cover a small fraction of the camera. Since all photons hitting the dead surface between the SiPMs would be lost, Winston cones (like one shown in Fig. 2.3) are used to collect the light on them. The shape and material of the Winston cones are such, that independent of the incident angle all photons entering the top surface are total reflected on the side surfaces. All photons leave the cone through the square bottom surface, which matches the size of the SiPM. The top surface is hexagonal in respect for the hexagonal orientation of the SiPMs on the camera plate, consistently covering the focus area of the fresnel lense. This particular design was developed at RWTH Aachen. [32]
The Winston cones are fabricated by turnery of a special UV-transparent plexiglass ("PLEXIGLAS XT Farblos 0A070 GT"). The expected gain in intensity g is the fraction of top (hexagonal, side-length 9mm) and bottom surface (square, side-length 6mm). Two different series of cones were used for this thesis - old and new ones fabricated by the workshop at FAU as well as an external laboratory (CNC Adam) respectively.
A two component glue (EPOTEK 310M-2) was used to fix the cones on the SiPMs. While the top and side surfaces of the cones are polished, small grooves in the bottom surface enable the glue to get in and improve stability. EPOTEK 310M-2 has a refraction index of 1.4947 which is very close to the one of plexi glass (≈ 1.5). [5] By that, scattering at the interface and therefore loss of photons is minimized.
The cones were cleaned with soap and flushed with deionized water before being fixed on the SiPM. Initially the glue has a low viscosity, which made it impossible to accurately glue neighbouring cones at a time. The fastest way is beginning with the middle pixel and then moving circular outwards, where every second cone of the circle is glued per

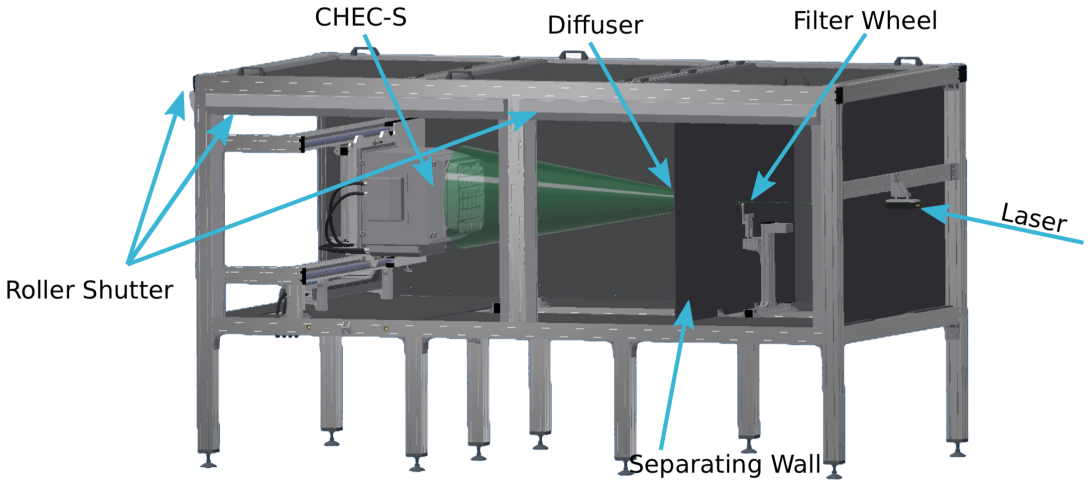

Figure 2.4: **Dark box design.** Dark box created for the test of compact high energy cameras (chec). A picosecond pulsed laser mimics the short Cherenkov showers. The intensity can be controled by tuning the laser and a filter wheel with different transmission coefficients. The beam partly hits a photodiode and its photocurrent in nA is a measure for the intensity of the radiation. After that, the laser beam is diffused with an angular dependence such that homogeneous intensity reaches the area of the tested camera in the back of the box indicated by CHEC-S. [23]

session. So just 9 sessions were needed for the inner 61 channels, leaving 44-46 without cone. Since the glue takes ∼20 h to dry under room conditions, the whole process took 9 days. For the later cameras, an under-pressure placer (at RWTH Aachen) was used. By that, the procedure was accomplished within 2 days and with much higher accuracy. The gain is defined as the factor by which the number of the photons that hit the SiPM is increased. For an ideal cone all photons get reflected on the side surfaces, which means that all photons that enter the top surface will hit the SiPM. Under the assumption of homogeneous illumination the expected gain

$$g = \frac{A_{top}}{A_{bottom}} = \frac{210mm^2}{36mm^2} \approx 5.85 \tag{2.1}$$

can be calculated by the fraction of top (hexagon with sidelength 9 mm) and bottom (square with sidelength 6 mm) surface.
To experimentally determine g, the camera is placed in a dark box designed by Benedikt Herrmann, shown in Fig. 2.4. A pico-second laser illuminates the whole camera plate with homogeneous intensity. Two such measurements were taken for several illumination intensities throughout the dynamic range of the SiPMs - one with and one without the cones. After a low pass filter was applied to the waveforms, a Gaussian fit to the signal peak determines the peak-height and the arrival time of the signal (chapter 3). The

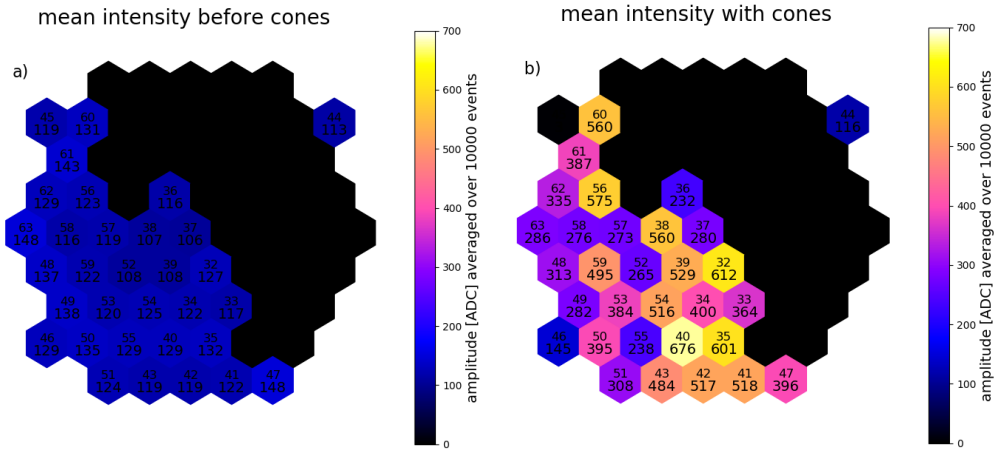

Figure 2.5: **Intensities with and without Winston cones.** Mean (10000 events), Gaussian fitted peak amplitude before (a) and after (b) gluing the cones at a laser intensity of 3nA exemplary for the old cones.

intensity distribution remained mainly independent of the incident light intensity and measurement, so just one measurement is displayed in Fig 2.5.
The gain g is the fraction of the mean pulse heights of both measurements and is displayed in Fig. 2.6. As mentioned, no cones where attached to Channels 44, 45 and 46. For both cameras 44 and 46 show values of roughly 1, which indicates that the two measurements indeed where under similar conditions. Due to the exact position of the laser and the incident angle of the photons, channel 45 was in the shadow of the cones on 60 and 61, which gives the explanation, why it has seen no intensity after the attachment of the cones. For the old camera channels 0 to 31 are blacked, since during the time of the gluing the shaper of the primary board was modified. Therefore the pure effect of the cones can not be obtained from these channels. The SiPM of channel 49 of the new camera broke on transport giving an explanation to the low gain value.
For all old cones an amplification can be observed, however, their quality shows large deviations. The best reach values up to ∼5.3, close to the theoretical maximum amplification of ∼5.8, while some values are even below 2. A correlation between a low g value and a brighter appearance in the photo can be obtained. Too high temperatures during the manufacturing process caused micro fissures, that scatter photons out of the cone. This is the reason why not just they appear brighter but also less laser photons reach the SiPM and they have a lower gain. Since the manufacturing machine run hot during the process, the effect is absent for the first cones being produced in a session. This explains the large deviation in quality.
The new cones are much more homogeneous. Despite a few exceptions, like channel 15 where again a bright appearance is correlated with a lower g, they all show values of average ~ 6.5. Surprisingly this exceeds the theoretical predicted amplification. A possible origin is that the measurements were taken without applying a transfer function. It is non-linear with the particular effect, that small amplitudes are estimated even smaller.

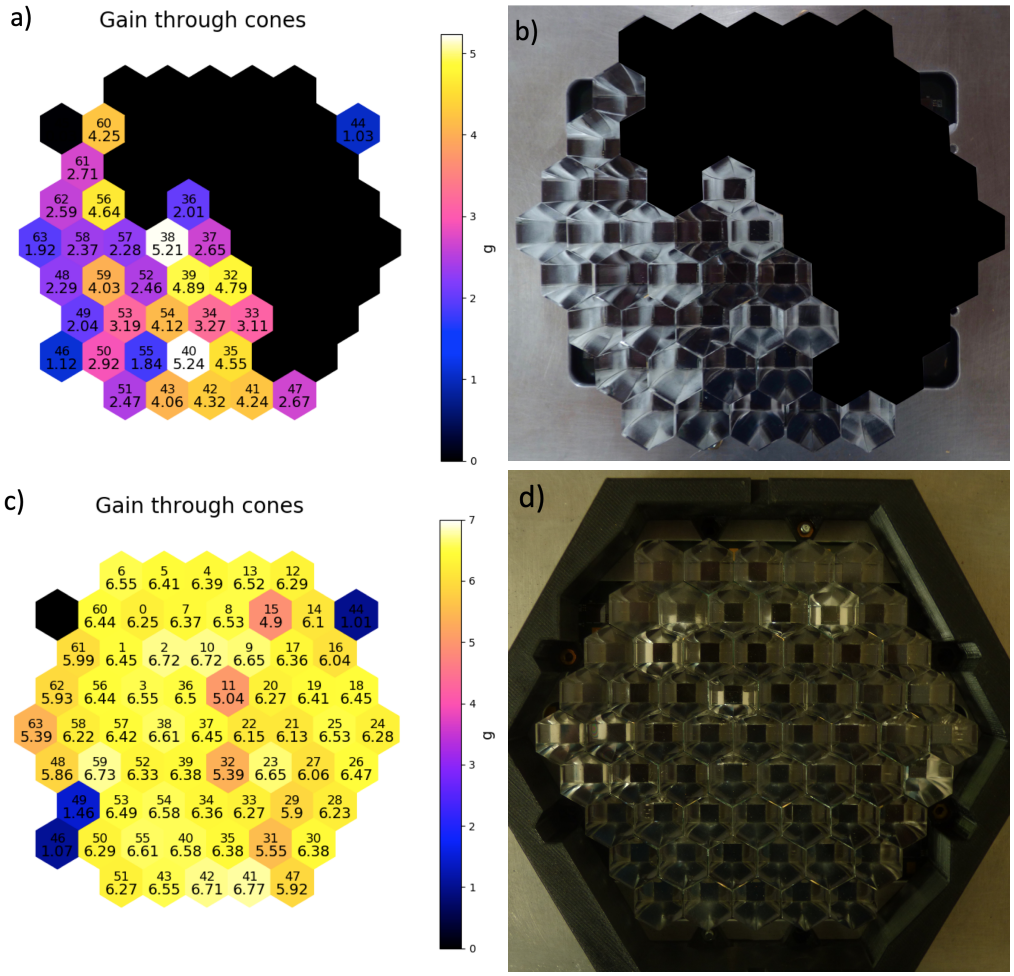

Figure 2.6: **Intensity gain through Winston cones.** Measured gain g and photo of the old (a,b) and new (c,d) cones. Channels 0-31 in old camera are blacked due to change of the shaper and therefore not the pure effect of the cones could be observed. The gain is determined by the factor between the mean amplitude of ∼10000 events with and without the cones under illumination with the same intensity.

Since a large amplitude with cones is divided by a smaller without, this leads to higher g values. This explanation is supported by the fact, that the excess of the theoretical maximum g decreases with rising initial amplitudes.

2.2 Camera

2.2.1 Silicon Photo Multipliers

Even though the Cherenkov light gets focussed, the signal from Air Showers remains weak ($\sim 10 - 200$ photons / pixel). In a photomultiplier the incident photon hits a target material and creates a photo-electron. It is accelerated by electric fields to sufficient energies to create secondary electrons, resulting in a measurable electronic signal. In a standard photomultiplier the electronic avalanche is accelerated through a sequence of cathodes in an evacuated volume. A silicon-photomultiplier (SiPM), which is a silicon p-n-diode operated in reverse direction, however, is much smaller, less fragile and needs less power.
The bias voltage causes a depletion region around the interface between p- and n-doped region, acting like an insulating layer. If a photo-electron is created in that region, it gets accelerated by the strong electric field induced by the charge separation in the depletion zone. If the bias voltage exceeds the breakdown voltage V_B, the electric field if sufficient to accelerate the electron such, that it creates an avalanche of secondary charge carriers. The SiPMs for this camera are SensL MicroFJ-60035-TSV. [2] Each of them consists of $\sim$ 20000 micro cells creating an avalanche of a distinct number of secondary electrons if hit. This, so called, gain g is typically on the order of $\sim 10^6$ and depends linearly on the over-voltage V_O, which is the exceed of the bias in respect of the breakdown voltage. In principle all the micro cells are independent of each other, but secondary photons can cause neighbouring cells to fire. This effect is known as crosstalk and ranges from $8 - 25\%$ per photon for over-voltages of $2.5 - 6.0$ V.
The electrons from all micro cells get summed up resulting in one electronic pulse per SiPM. Typical features are a sharp rise followed by a long decaying tail. By knowing the over-voltage or the gain respectively, one can determine the number of fired micro cells and by applying a correction for the crosstalk the number of photons hitting the SiPM.

2.2.2 Structure

16 different HVs can be applied to the camera - one to each group of 4 pixels. This matches the number of pixels included in one trigger group, which is the reason why for this particular camera they were chosen to be identical and named superpixels (indicated by the color code in Figure 2.7). To connect the camera with the TARGET module almost 300 contacts were applied by hand. This obviously contains a high potential of mixing them up and two simple tests ensure they are all in the right place.
For testing the right placement of the superpixel contacts just one of the 16 HVs was

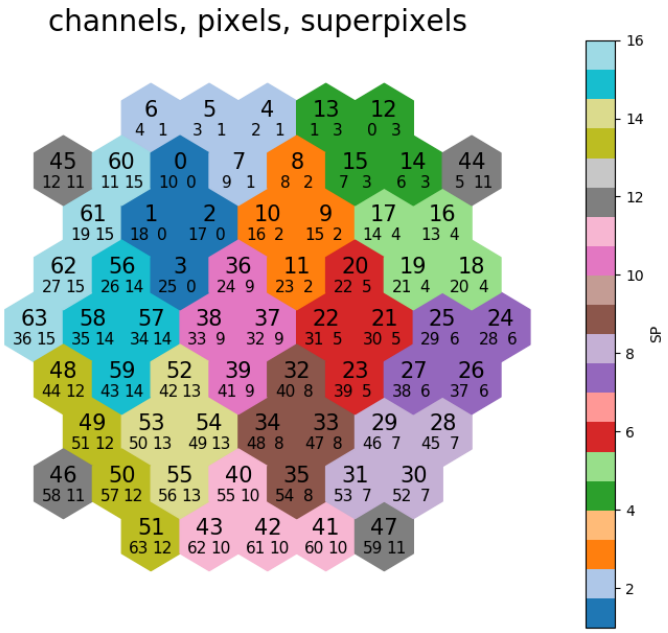

Figure 2.7: **Pixel configuration of the camera.** Upper number refers to readout channel on the TARGET board, lower left number indicates pixel number given on the camera board and lower right number gives the trigger group number it belongs to.

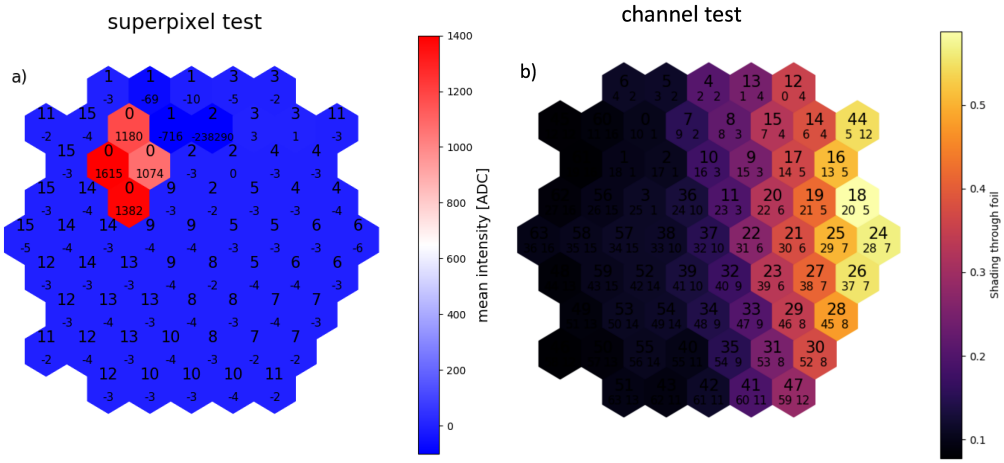

Figure 2.8: **Contacting HV application and signal readout.** (a) Test of superpixels (SP0). Upper number indicates the superpixel, lower the mean amplitude of 10000 events in ADC counts. (b) Test of single channels with a gradient foil. Numbers are channel, pixel, superpixel as in Fig. 2.7.

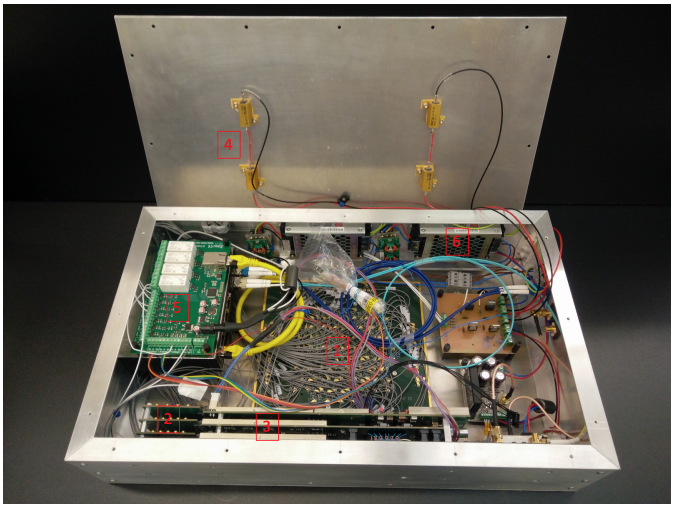

Figure 2.9: **Data aquisition box.** The camera is located on the bottom (1) and grey cables connect it through the adapter board (2) with the TARGET module (3). All the electronics, including the heating circuits (4), can be remotely controlled by a Relais card (5). DC-DC converter (6) ensure the power supply.

switched on at a time and illuminated with pulsed laser radiation. The SiPMs operated above breakdown voltage measured a clear signal, while the rest remained dark. The result for superpixel 0 is displayed in Figure 2.8 (a).
To test the single channel contacts is more complicated since there is no intrinsic difference between the pixels. A shading foil was created by printing a gradient from transparent to black along one axis on a transparent foil. Two measurements in the dark box under the identical laser illumination were taken - once clear and once with the shading foil horizontally placed directly in front of the pixels. Building the fraction between the two measurements cancels out all other effects and the pure shading of the foil is displayed in Fig. 2.8 (b). The shading factor nicely represents the gradient of the foil, so it is assumed, that all channels work and every contact is in the right place.

2.3 Readout Electronics

All the electronics are located in an aluminium box right below the camera (Fig. 2.9), which makes the telescope compact and less fragile.

2.3.1 Pre-Amplifier

Before the signal reaches the TARGET module it is modified right after the SiPM. An amplifier (Linear Technologies, LHM6714) transforms the weak current signal into a

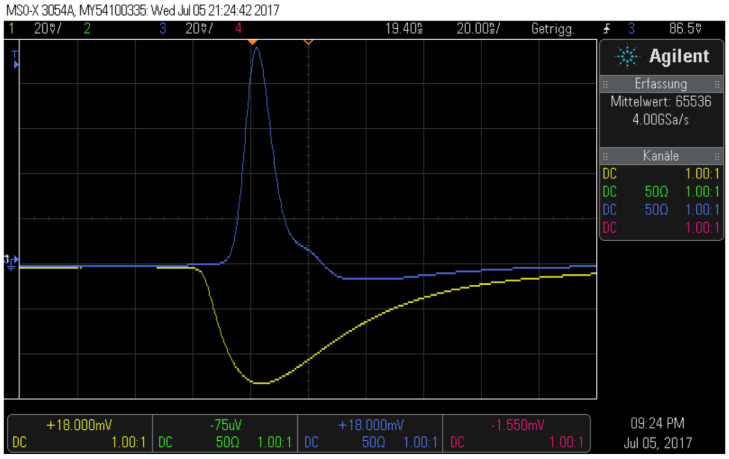

Figure 2.10: **Shaping of signal pulse.** Oscilloscope image of the signal pulse before (yellow) and after (blue) the shaper averaged over 65536 pulses. The long tail of the SiPM output pulse gets shortend to avoid pile-up. The upward dip after the blue peak is no real feature, but a trigger artefact caused by the oscilloscope. [29]

higher voltage pulse, which is less susceptible to noise.

2.3.2 Shaper

Besides the weakness, another characteristic of a SiPM pulse is a sharp rise followed by a long decaying tail ($\sim$ 100ns). To avoid pile-up effects the pulse gets shortened by a parallel connection of a capacitor and resistor. The signal from the capacitor has sharper rise and fall times, however, it is bipolar and features a large undershoot (double Landau pulse). The positive pulse from the resistor compensates (at least partly) for this effect. Since it is also added to the positive part of the capacitor signal, it increases the pulse height. A comparison of the signal pulse before and after the shaper is shown in Fig. 2.10. Different configurations of resistors and capacitors were tested by Kristof Kremer and the one proofed to be the best resulted in an amplitude amplification of ~ 2. [29]

2.3.3 TARGET C

The amplified and shaped signals from the SiPMs are read out by a TARGET C module (Fig. 2.11). It features an individual electronic channel (upper number in Fig. 2.7) for all 64 pixels (lower left number in Fig. 2.7).
The amplified and shaped signal then goes into the TARGET module. The TARGET modules are a series of readout boards by application specific integrated circuits (ASICs) designed for IACTs. In the latest version the ASIC for sampling, buffering and digitizing

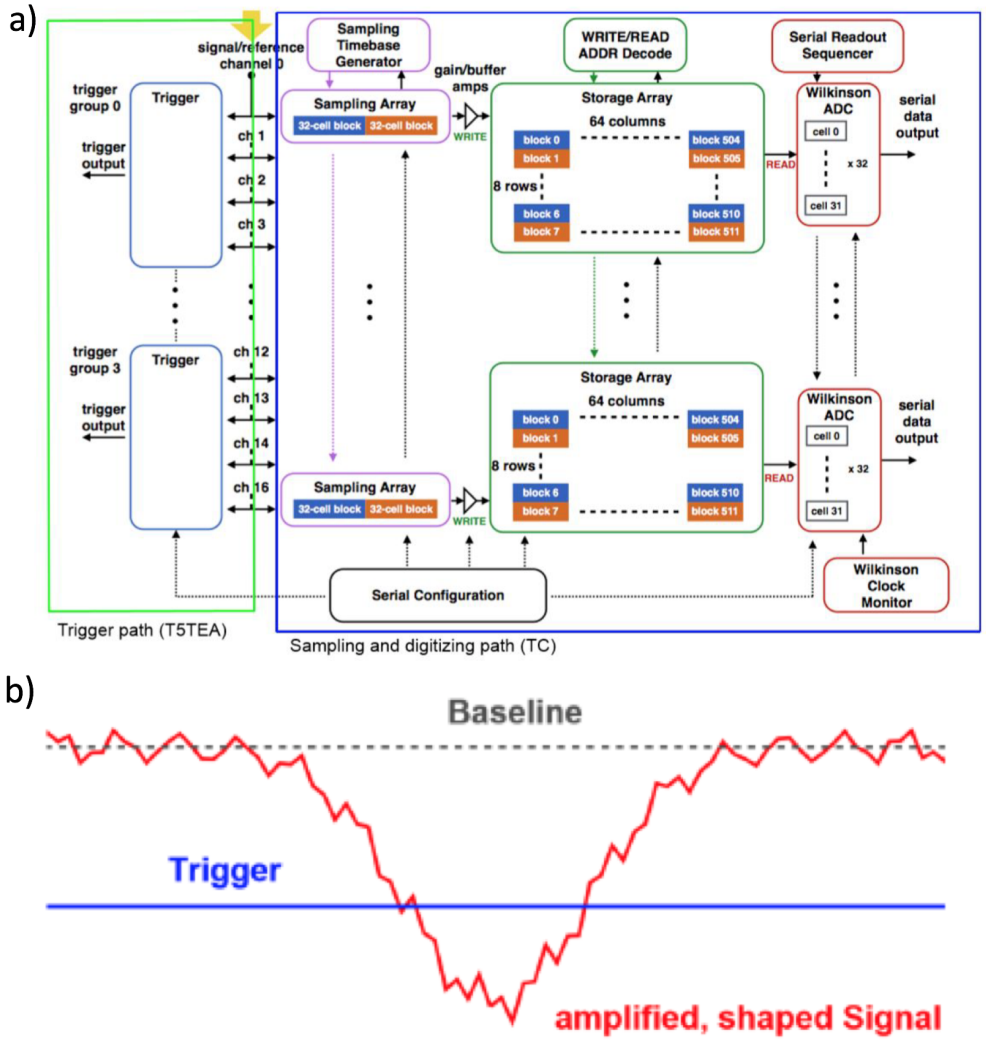

Figure 2.11: **Readout electronics.** (a) Electronic paths inside the TARGET. Halfcycles of the sampling array allow for sampling with 1 GHz. 16384 capacitors in storage array buffer $\sim 16\mu$s from which a maximal time window of 512 ns is digitized by a Wilkinson ADC if a trigger occured. [36] (b) Trigger illustration. Increasing the parameter PMTref4 shifts the baseline upwords, increasing the trigger threshold. Adjusting the threshold with the parameter Trgthresh has the opposite effect, since the signal is inverted. [35]

(TARGET C) is separated from the ASIC responsible for triggering (T5TEA), which reduces the crosstalk between sampling and trigger path, while the charge resolution and the dynamic range are retained. [20]
The shaped output signal of the SiPMs arrives at the sampling array of TARGET C (Fig. 2.11 (a)), which consists of 64 capacitors forming two sampling blocks of 32. While one block samples the signal from the SiPMs, the other block is written to the storage array. After one half-cycle this process runs reverse, allowing for continuous sampling with 1GHz.
The storage array consists of 16385 capacitors, allowing for data storage up to $\sim 16\mu$s giving an upper limit on possible trigger delays. This is just relevant for telescope arrays, since the internal delays of a single camera, as examined in this thesis, never exceed 1μs. The trigger flags a sample in the storage, in which case a range of samples, referring to a time window of maximal 512 ns shifted by an adjustable trigger delay, is digitized by Wilkinson ADCs including a time stamp.
The TARGET module features different triggers. For internally triggering on the waveforms, the same shaped signal from the SiPMs arrives at the T5TEA ASIC. After being inverted, the analogue sum of four channels of one trigger group (lower right number in Fig. 2.7) is compared to a threshold (Fig. 2.11 (b)), which is controlled by a parameter Trgthresh. To stay in the operational range of the comparator, an additional parameter PMTref4 shifts the baseline such, that the negative peak still remains on positive voltages. It follows, that increasing PMTref4 increases the trigger threshold while Trgthresh has the opposite effect. The internal dead-time allows for a maximum trigger rate of ~ 10 kHz.
As a summed signal of a trigger group exceeds the threshold, a trigger pulse of 20 ns is created. A clock tests the trigger pulse every 8 ns with a distinct deadtime after recording an event. If triggering on coincidence (with coincidence level c_1), the 8 ns clock tests whether more or equal c_1 of trigger groups exceeded the threshold at a time.
The NSB photons arrive randomly, while the photons originating from an air shower are bundled within few nanoseconds. Additionally, the showers are extended on the night sky and are likely to hit more than one trigger group. As a consequence, the signal to noise ratio is improved tremendously.
TARGET additionally features an external trigger input. Applications are telescope arrays, where one telescopes internal trigger triggers the others, or to observe together with radio or scintillator (IceSCINT) measurements. It was also used to test the camera under pulsed laser radiation. Every time the laser emits a light pulse, an electronic pulse is sent to the external trigger to ensure a time window around the photon pulse is digitized.
A trigger delay compensates for the electronic delays in both cases and has to be set for internal and external trigger individually.

3 Analysis

This chapter is about the processing of the digitized shaped waveforms. It also contains a low level analysis used for the majority of measurements in this thesis.

3.1 Waveform processing

Fig. 3.1 shows a typical, digitized waveform as it leaves the TARGET module. Before and after the signal peak the waveform is, more or less, contantly 0 due to pedestal calibration. [29] The signal peak features a sharp rise and fall with a minimized undershoot after the pulse, as expected after the shaper (section 2.3.2).
By applying a suitable low pass filter (band pass frequency ~ 80 MHz), high frequency noise can be cancelled and the waveform becomes smoother. Fig. 3.1 also shows, that the important properties of the signal peak, in particular height and position, are preserved.

3.2 Low level analysis

For analysis of the recorded waveforms, a Gaussian function is fitted to the filtered signal peak (Fig. 3.2). Three starting parameters are required for the fit. For the pulse height and position the highest sampled amplitude and its sample position respectively were chosen. The peak-width had minor impact and was set to 3 σ.
Even though the pulse is double Landau shaped (sec. 2.3.2) good results can be obtained from a Gaussian approximation. For the peak-height (zoom in Fig. 3.2), for example, the difference is lower than 2 ADC counts. With a gain of $\sim 6 - 8$ ADC counts this refers to an error of ~ 3 % and is therefore an effect lower than 1 photo electron (p.e.). The displayed waveform features with ~ 60 ADC counts (referring to ~ 10 p.e.) a comparably small peak-height. For higher pulses the relative error is significantly smaller, dropping below 1% at a still small peak-height of 200 ADC counts.
Saturation is reached somewhere around ~ 3100 ADC counts. The waveform maximizes at this value, however, the Gaussian fit exceeds it, partly compensating for the saturation. Such an analysis occasionally shows higher peak-heights than saturation allows, however, it is far off the real peak-height and according number of incident photons. For better reconstruction of the saturated range the length of the raised plateau after the peak could be used, however, this was still under investigation by Manuel Loos at the time this thesis was published.

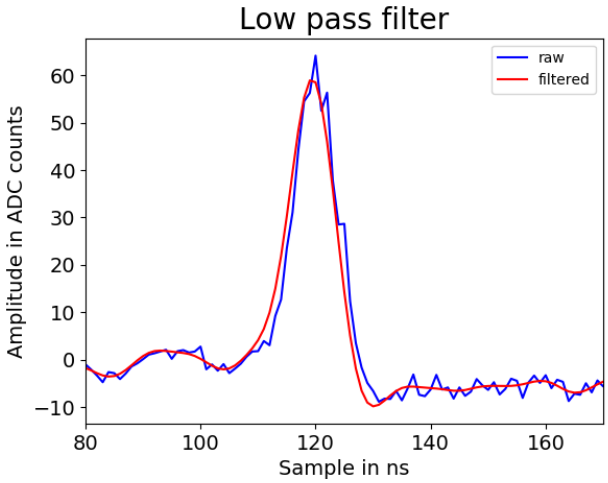

Figure 3.1: **Low pass filter.** A low pass filter is applied to the raw waveform to reduce high frequency noise.

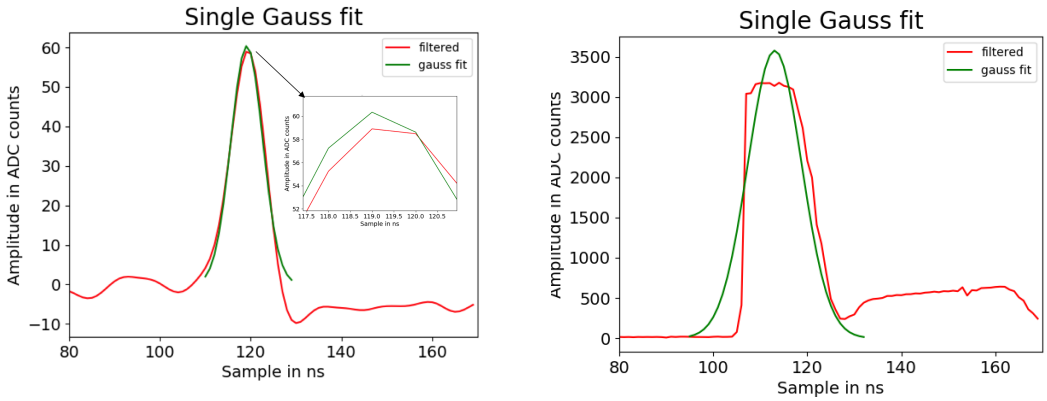

Figure 3.2: **Single gauss fit.** A single Gaussian function (green) is fitted to the filtered signal peak (red). For the unsaturated case (a) the fit matches the waveform reasonably well with an error of $\sim$ 2 ADC counts referring to a sub p.e. effect, This is even better for higher peaks than the displayed one. If the pulse saturates (b), the fit partly compensates for the cut-off at $\sim$ 3100 ADC counts, resulting in higher peak-heights than saturation. This, however, does not reconstruct the peak-height and the real number of incident photons well.

From the fitted parameters, the most basic properties can be obtained. The pulse height is referred to an intensity. Divided by the gain it gives the number of photons detected in one pixel. By summing the intensity of all pixels one gets the size, which is the closest one gets to an "energy" with this low level analysis. The mean position of the pulse gives the mean arrival time of the photons.
Although this type of analysis is rather elementary, it was sufficient for the measurements for this thesis.

4 Calibration

The waveforms are already pedestal calibrated. Nonetheless, inhomogeneities of the intensity or the signal time between the pixels remain. They result from hardware differences like deviating breakdown voltages of the SiPMs or different electronic path lengths, respectively. However, these errors are independent of measurement time and parameters and so can be corrected for by applying templates.

4.1 Intensity

After all previously discussed effects and contributions, the pixels show very different intensities under similar radiation (laser intensity deviation less than 5%). However, the fractional deviation of the intensity of each pixel from the mean value of all remains constant over time and different intensities. This allows to use one single template to correct for this inhomogeneity.
Eight measurements at two different days were taken. The photocurrent, corresponding to the laser intensity, was 0.5nA, 1nA, 3nA and 6nA respectively, well covering the dynamic range. The signal pulse was Gaussian fitted for 10000 events each (chapter 3) and the mean value of the determined heights $\langle h \rangle_{\text{pixel,meas}}$ identified. The intensity correction factor obtained per pixel from one measurement

$$i_{\text{pixel,meas}} = \frac{\langle h \rangle_{\text{pixel,meas}}}{\langle \langle h \rangle_{\text{pixel,meas}} \rangle_{\text{pixels}}} \tag{4.1}$$

is the mean peak-height of this pixel divided by the mean value of all peak-heights of this measurement. The overall intensity correction factor per pixel

$$i_{\text{pixel}} = \langle i_{\text{pixel,meas}} \rangle_{\text{measurements}} \tag{4.2}$$

is then the mean value of all the measurements. The resulting template is shown in Fig. 4.1(a). Fig. 4.1(b) shows an additional measurement, that did not contribute to the calculation of the template after being corrected with it. Excluding the channels 44-46 good homogeneity is achieved, since - except for channel 63 - the maximal observed deviation is 10%.

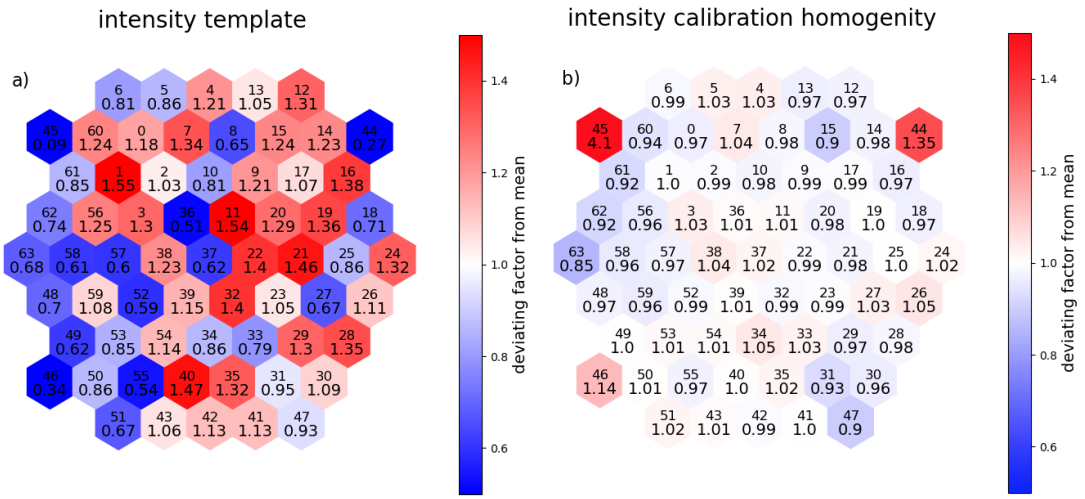

Figure 4.1: **Intensity template.** Intensity template obtained from 8 measurements covering as well time and dynamic range (a). Intensity deviations of an additional measurement under homogeneous illumination, not contributing to the template, after the correction (b).

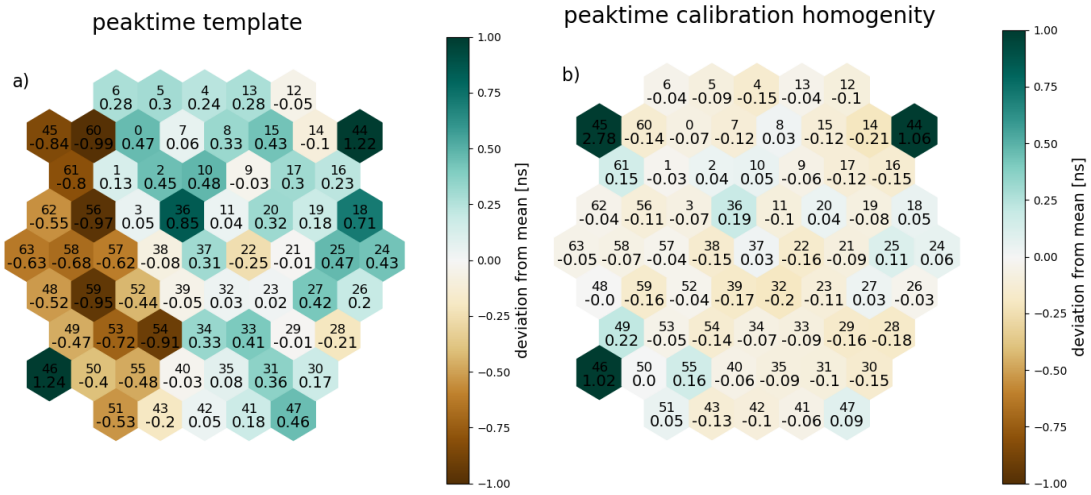

Figure 4.2: **Peak time template.** Peak arriving time template obtained from 8 measurements covering as well time and dynamic range (a). Arriving time deviations of an additional measurement under homogeneous illumination, not contributing to the template, after the correction (b).

4.2 Signal peak time

The arrival time of the peak, and in particular the differences to the other pixels, is of interest as well. Different travel times, caused dominantly by different path lengths in the TARGET module, cause a systematic error which can be corrected for in a similar way as discussed in the previous section.
The camera position was in the middle of the diffused laser beam, which means, that the light hits the central pixels earlier. From geometrical calculations one obtains a time difference $\Delta t \approx 0.01$ns - just 1 % of the sampling time and therefore negligible.
The same eight measurements were taken as for the intensity calibration with the difference, that the peak-positions - not the heights - from the Gaussian fits were examined. Again the mean values per pixel $\langle t \rangle_{\text{pixel,meas}}$ were determined from 10000 events each, however, the deviation of the single pixels to the mean value

$$\Delta t_{\text{pixel,meas}} = \langle t \rangle_{\text{pixel,meas}} - \langle \langle t \rangle_{\text{pixel,meas}} \rangle_{\text{pixels}} \tag{4.3}$$

is no longer the fraction, but obtained by subtracting. The reason is, that the electronic delay is corrected for by displacing the time range of the sampling. The resulting template is again the mean of all taken measurements and is shown in Fig. 4.2, together with its application on the additional measurement. The deviations between the channels are now on the order of $\sim$0.3ns. Since theory (section 1.2) predicts and measurement (section 7.1) confirms evolution times on the order of several ns for the majority of the showers this can be considered good enough.

4.3 Muon calibration

As an atmospheric muon hits the Winston cones, it produces Cherenkov photons along its trajectory. In principle these muons could be used to create templates for intensity and peak-time with the great advantage, that they arrive homogeneously at every point on earth.
In a muon signature just one or very few connecting pixels are hit, however they show a comparably large amplitude of typically $100 - 200$ p.e. Since muons can be observed with a light shield right above the camera, light pollution and therefore the noise level is very low. This allows to trigger on a threshold of ~ 10 p.e. even without coincidence of superpixels to observe these muons.
The number of created Cherenkov photons, however, shows various dependencies. It is affected by the energy of the incident muon as well as the length of the trajectory through the cone. Latter shows great differences under varying incident angles due to the extraordinary shape of the cones. This is the reason why very high statistics (and therefore long measurements) would be required for sufficiently covering the whole parameter space to achieve good homogeneity of the templates.

5 Constant gain correction

One goal on the way to achieve uniform data is to keep the gain constant. By that, a distinct peak-height always corresponds to a certain amount of p.e. The gain per p.e.

$$g = \alpha \cdot V_O = \alpha \cdot (V - V_B) \tag{5.1}$$

is proportional to the over-voltage V_O, and therefore the applied voltage V subtracted by the breakdown voltage V_B of the SiPM. Latter is temperature dependent and potentially underlies changes during a measurement. One way to correct for that effect is to apply a new voltage V_n such, that $V_n - V = \Delta V_B$. In the following g_s is the value on which the gain should be stabilized.

5.1 HV Application

As mentioned in section 2, the high voltage (HV) is applied to the SiPMs by a digital-to-analogue converter (DAC). The applied voltage was measured for all DAC values and each of the 16 potentiometers.
Fig. 5.1(a) shows the well matched linear dependence of the applied voltage on the the DAC value. The deviations between the different potentiometers of ~ 0.3V can be obtained from Fig. 5.1(b). Since the DAC values allow to set the HV with a precision of less than ~ 0.03V the different potentiometers were treated separately and the voltage set from a lookup-table for each of them.

5.2 Gain determination

The gain can be determined from dark counts in the triggered events. Since always four channels are combined in one trigger group and the same voltage is applied to them, just the mean gain of each superpixel can be corrected for. Therefore the gains of the 4 channels within one superpixel are determined separately and their mean is taken.
The dark counts are taken from the triggered waveforms, in particular just those before the signal peak, due to post-pulse oscillation and other such effects. Peaks in the first 10 samples can not be used either, since uncertainties in the later performed Gaussian fit can occur. Peaks were detected with the scipy.signal function `find_peaks_cwt`. Due to the earlier discussed low-pass filter the number of peaks per event is handy, but still contains noise fluctuations. Fig. 5.2(a) shows noise and dark counts of an exemplary channel in the observed time range. A threshold of 4 DAC counts proved to be the best

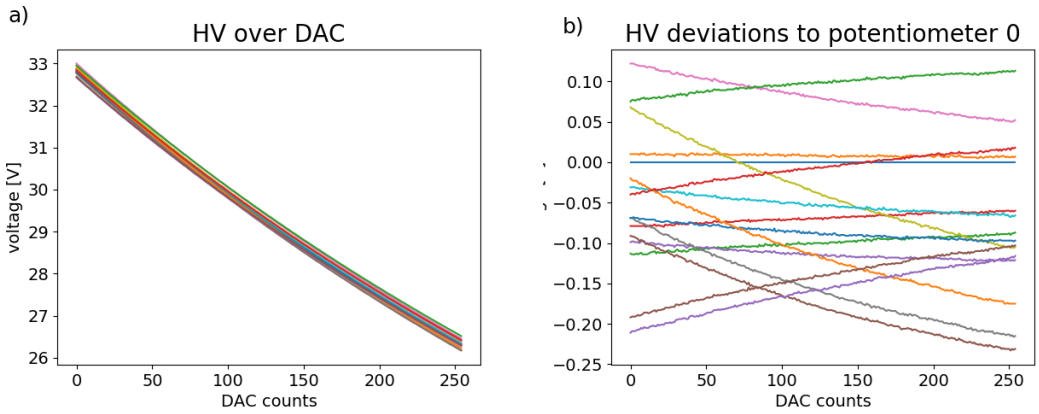

Figure 5.1: **Applied voltage over DAC value.** The measured applied voltage to the SiPMs of the potentiometers depends linear on the DAC value (a). The deviations of the potentiometers to an arbitrary chosen 0 one at each DAC value (b).

ruling-out criterion.
The remaining peaks are believed to be dark counts and their positions (as found by the peak finder) are shown as red dots in an exemplary waveform in Fig. 5.2(b). SiPM pulses are Gaussian shaped, so such a fit is performed around the peak-finder positions to determine the peak-height. The initial parameters had just a minor effect on the fit result and e.g. height / position could be obtained from the waveform values at the peak-finder position. This is not the case for the time window that was fitted. If it is too small, one underlies the risk, that the peak-finder position differs too much from the real maximum, while a too big window results in a strong noise contribution. Best results were obtained for a fit window of 10 ns centred around the peak-finder position. The amplitude of the fitted gauss, however, is not yet the real dark count amplitude, since the baseline underlies short time changes the pedestal calibration can not correct for. It is determined simply by the mean value of the waveform in absence of any dark counts or signal peaks, since statistical noise is believed to cancel out. This interval was chosen from the first sample up to 10 samples before the first dark count position, to assure that no parts of the dark count peak influence the baseline. The real peak-height then is the obtained amplitude of the Gaussian fit subtracted by the baseline value. An alternative to the Gaussian fit, though not performed in this thesis, would be to take the area of the pulse.
The obtained peak-heights are binned and shown in one histogram for each channel Fig. 5.2(c) . The spectrum is dominated by the single p. e. peak (the first in the histogram since the 0th peak was cut) since dark counts always create one electron-hole pair inside the Si diode and therefore act like one photon. Nonetheless, at least for a certain amount of events, the higher order peaks are visible. This is due to crosstalk inside the SiPM and is useful, since one can perform a multi-gaussian fit. Due to the probability for crosstalk the expected peak-widths decrease with a factor of $\frac{1}{\sqrt{n}}$ for the nth p.e. peak.

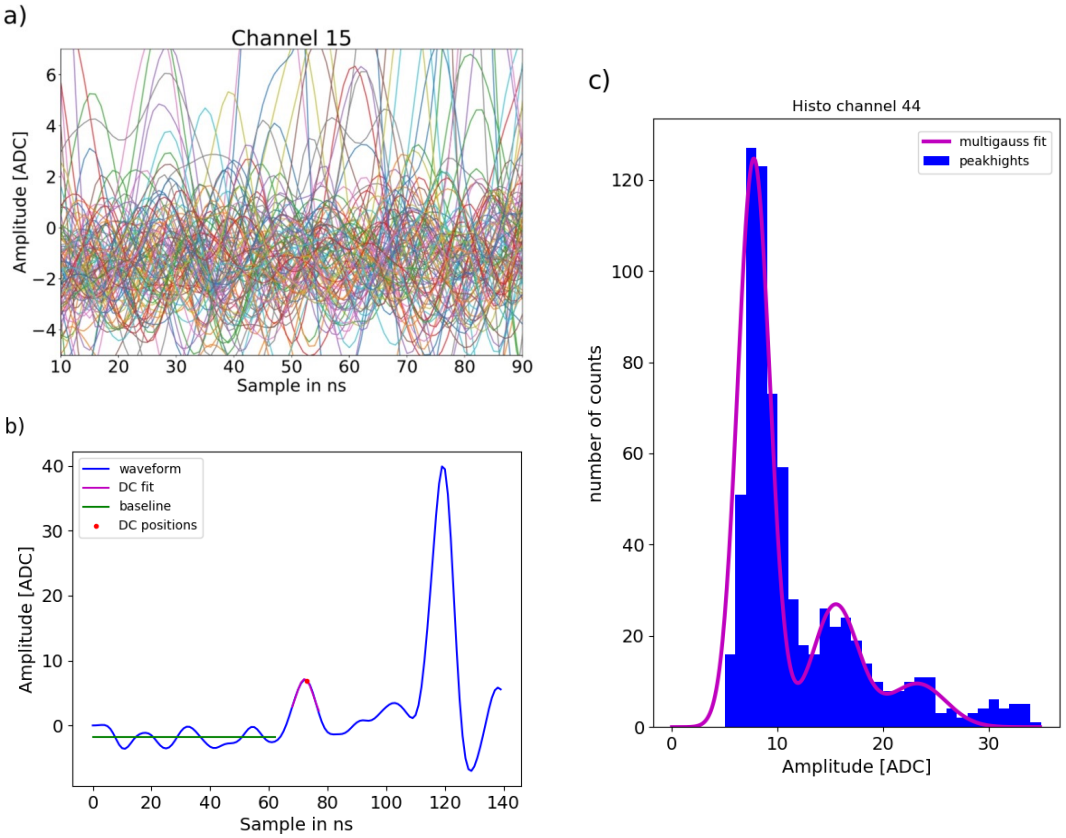

Figure 5.2: **Gain determination from dark counts.** Measurement was taken in the dark box under laser radiation with an intensity of 1 nA and the low-pass filter was applied to the data. (a) 100 events plotted in the for dark counts examined range. Threshold on noise determined to 4 ADC counts. (b) Typical single waveform plotted up to the signal peak. Dark count positions determined by the scipy peak-finder. The Gaussian fit of the dark count peak as well as the fit of the baseline can be observed. (c) Histogram of the determined peak-heights of a single channel from 2000 events. The distance between the peaks of the multi-gaussian fit determines the gain. For this channel even the fourth peak is visible, but due to the low count numbers it underlies great uncertainties and, therefore, does not contribute to the gain determination.

For a fit up to the 3 p.e. peak the function has then the shape

$$f(x) = a_1 \cdot e^{-\frac{(x-b)^2}{2c^2}} + a_2 \cdot e^{-\frac{(x-2b)^2}{2(\sqrt{2}c)^2}} + a_3 \cdot e^{-\frac{(x-3b)^2}{2(\sqrt{3}c)^2}}. \tag{5.2}$$

The initial parameters for the heights of the peaks had no impact on the fit, as well as the initial value of width c. For the position b g_s was used as a start value.
The distance between the peaks, or the fit parameter b, is the measured gain determined with gaincontrol and from now on named g_m.

5.3 Stabilizing the gain

The gain can be stabilized for all superpixels individually. At first one determines

$$\Delta g = \frac{g_m}{g_s} \tag{5.3}$$

the deviation of the measured gain to the gain value that should be. Since the gain is proportional to the over-voltage

$$\Delta V_O := \frac{V_{O,n}}{V_O} = \frac{V_n - V_{B,n}}{V - V_B} \stackrel{!}{=} \frac{1}{\Delta g} \tag{5.4}$$

the new over-voltage $V_{O,n}$ over the old V_O should give the inverse value and therefore a criterion for the new voltage V_n, that has to be set. Even though $V_{B,n}$ is unknown due to temperature dependency it can be assumed that $V_{B,n} = V_B$. With this simplification equation 5.4 can be solved for the new set voltage

$$V_n = (V - V_B) \cdot \frac{1}{\Delta g} + V_B. \tag{5.5}$$

As long as $V > V_B$ the voltage, and the gain, are adjusted with the right sign and can count as valid. However, any deviation of V_B to the actual breakdown voltage lead to a longer time until the stable regime around g_s is reached. The larger this deviation is, the larger this effect.
The breakdown voltage changes with $\sim$ 21.5mV per ^{o}C [2]. Due to stable conditions of the polar night a temperature difference of 30^{o}C during one measurement is rather overestimated. Even for that case the error on the breakdown voltage $\Delta V_B \approx 0.65$V, which can well be taken as a lower limit on the operational overvoltage. This leads to a lower limit on g_s of $0.65V \cdot 1.41V^{-1} \approx 0.92$ [29]. This is well below any reasonable operational gain ($\sim$4-8) from which the validity of the assumption follows for all practical cases.
Gaincontrol was applied to a measurement in the dark box. The gain was determined from dark counts of 4000 events. The development of the gain of each superpixel during the time of the measurement is displayed in Fig. 5.3. Initially the same voltage of 30.4V was applied to all superpixels and the mean gains cover a range between 7.0 and 9.8, potentially resulting from differences of the breakdown voltages between the SiPMs. Even after a few cycles they are much closer to the set gain of 8 and after $\sim$1000s a final stable

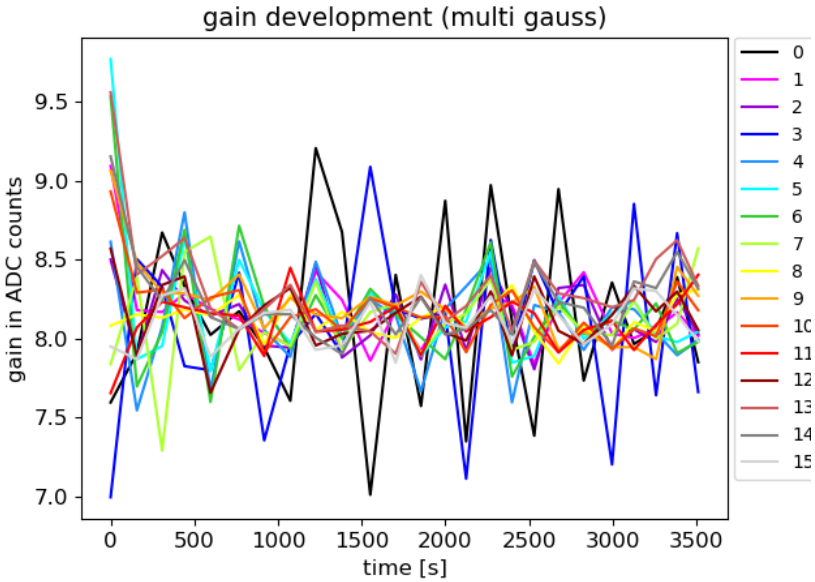

Figure 5.3: **Gain stabilization.** Determined gain of all superpixels over the time of the measurement with gaincontrol on a $g_s = 8$ ADC.

state is reached, where most of the superpixels deviate by less than 5%. Superpixels 0 and 3, however, show an overshoot which indicates an overcorrection.

6 Temperature sustainability

The IceACTs main application is planned at the South Pole. Promising advantages of this location, like very low light pollution or consecutive dark-time during the polar night, come at the cost of the harsh conditions - in particular the cold. Rather common temperatures around -50^{o}C (with peaks down to -70^{o}C or even below) give a real challenge to solid structure and electronics.

6.1 Cool-Chamber Test

The whole system (like described in section 2) was taken to RWTH Aachen and placed in a cooling container, shown in Fig. 6.1. The lowest temperature reached in the container was -48^{o}C. Since the majority of electric devices are rated down to -40^{o}C this is a good indicator whether the telescope will work under polar conditions.

6.1.1 Electronics

If running, the electronics consume power and heat the DAQ box. To simulate the most extreme case a cold start of the electronics - in particular the TARGET Module - was performed. Fig. 6.2 shows the temperature development on the TARGET Module, at the camera and on the bottom of the DAQ box.
After $\sim$12 hours in constant outside temperature of -48^{o}C the whole system was cooled to almost that value, where TARGET was successfully switched on. Immediately the power consumed by the module started to heat it, leading to a sharp rise of the temperature. The camera and the box show rising temperatures as well, however, the effect is significantly slower, since they are due to conduction of the heated air around the TARGET module. The temperature of the camera rises faster than of the bottom of the box, because the comparable hot air prefers to rise up towards the SiPMs.
A fan inside the box, located close to the TARGET module, is rated down to -10^{o}C and as the temperature of the module reaches that value it is switched on. This results in an increase of air convection, which distributes the heat produced at the TARGET module in the DAQ box. Therefore the temperature of the box shows a steep rise, while for the TARGET module the opposite is the case. Even the camera shows a slight decrease in temperature since the hot air from the TARGET not longer rises directly towards it.
After another while the whole camera shows constant temperature, indicated by the merging curves of the camera and the bottom of the box sensors. The TARGET Module still creates heat and therefore is hotter than the rest of the box. With this delta being

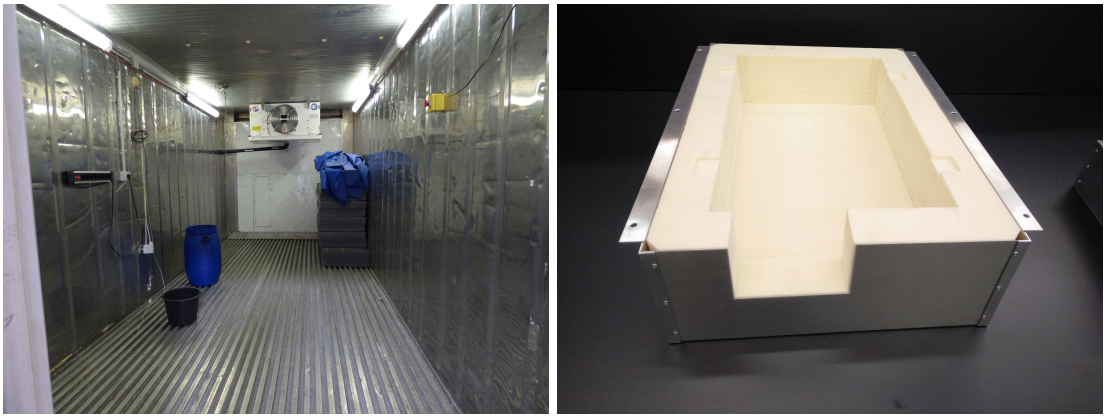

Figure 6.1: **Cold test setup.** Telescope in cooling container at RWTH Aachen. The DAQ box is isolated by a layer of isolating rigid foam (URSA XPS D N-III-PZ-I).

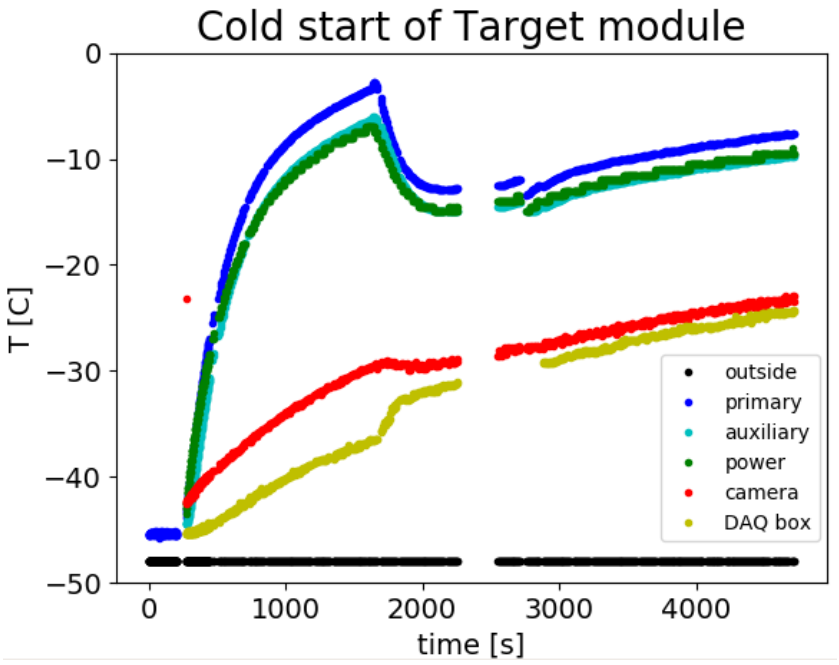

Figure 6.2: **Cold start of the Electronics at -48^{o}C.** Primary, auxiliary and power board are located on the TARGET module right below the camera with the SiPMs. One more temperature sensor is located at the bottom of the DAQ box. The temperature is logged for a cold start of the electronics at -48^{o}C. After ∼1600 s a fan inside the DAQ box is switched on.

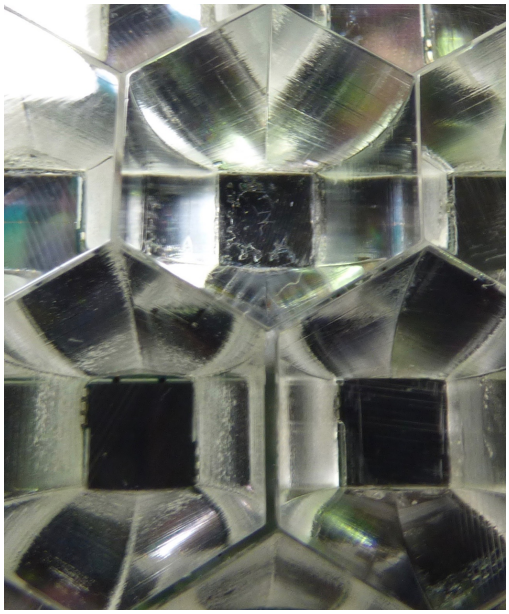

Figure 6.3: **Temperature test of solid structure.** Top view of some Winston cones. Thermal stress of the glue between the Winston cones and the SiPMs degenerated the glue of the cones.

constant the whole system is heated towards a stable state, leading to a temperature difference between the TARGET Module and the outside of $\Delta T \approx 40^o$C.
The observed behaviour of the temperatures inside the box matches the expectations. Together with the successful measurement of muons described in section 6.1.3, it allows for the conclusion that the electronics work well even under these extreme conditions. As long TARGET is running, the ΔT promises even for the coldest conditions a TARGET module temperature of at least -30^oC, which is well above the rating. Beside a long power outage combined with extremely low temperatures, which is the only case that could not be simulated due to limits on the cooling container temperature, the test proofed that the electronics of the telescope are ready to work in the extreme conditions of the polar night.

6.1.2 Solid structure

The telescope is mainly composed of thermally resistant materials like aluminium, carbon or glass and is very resilient to thermal stress. However, the cold had some impact on the glue of the SiPMs.
After the telescope was taken out of the cooling container, at 6 out of 64 Winston cones degeneration of the glue was observed. This effect is shown in Fig. 6.3 (a), where the upper cone shows white corrugations, whereas the lower ones appear smoothly black.
The physical strength of the glued connection was tested by gentle mechanical stress

applied to some corner cones. While all smooth cones survived the procedure, the only cone showing the degeneration fell off. Closer examination of this cone revealed, that the glass coverage of the SiPM was still fixed to the bottom of the cone, however, the glue that agglutinates the glass and the silicon layers inside the SiPM showed the degeneration and failed.
There are several possible explanations for this effect. Apparently the SiPMs were cooled below their minimum operational temperature of -40^oC. [2] Still, that alone seems unlikely to be the explanation, since identical SiPMs were cooled to $\sim -60^oC$ with liquid nitrogen without showing any degeneration. [16] This leads to the assumption, that this effect just occurs in combination with the cones.
A likely explanation is thermal stress. Since every material deforms differently under temperature change, large temperature and expansion coefficient differences can cause great forces at the interfaces. If the SiPMs are sandwiched between the camera plate and the Winston cones, the top and the bottom surface of the SiPMs are fixed and the force inside it increased. This can lead to the breaking of the weakest layer - presumably the glue between the glass and the silicon.
Another possibility is a chemical solvation of the glue inside the SiPM. As long the EPOTEK glue dries out it evaporates solvent. If excessive glue runs down to the glue in the Winston cone the evaporation might soften it. As the EPOTEK dries it contracts, potentially weakening the softened glue. This would at least contribute to the breaking under thermal stress. Even though SensL did not reveal the exact composition of the glue inside the SiPMs, they did not exclude this possibility. [15]
Thermal stress seems to be the most likely explanation, but at this point the exact origin of the effect remains unclear. Testing different glues could reveal it and potentially solve the issue.

6.1.3 Muon Measurement

The hardware of the telescope (almost exclusively) endured the test in the cooling chamber, however, the most crucial question remains, whether the software runs as expected. Apparently no air shower induced Cherenkov light can enter the cooling box and so measuring Cosmic Rays can not serve as a test. However, high energy muons are not shielded by the outer walls of the cooling container and qualify for such a test.
In most cases the trajectory of the muon passes just one or two cones and therefore illuminates just one or two pixels. This makes it unlikely to trigger two superpixels and limits one on measuring without coincidence. Besides the already low noise due to the absence of night sky background (NSB), the low temperature of the SiPMs lead to a low dark count rate and a very low noise level. Consecutively it was still possible to trigger on a threshold of 10 p.e., which is well below the number of Cherenkov photons induced by muons with an energy of reasonable event rates.
An event rate of 3.3 Hz was obtained with less than 1% noise triggers. Fig. 6.4 shows an example event of this measurement. Two pixels show a strong signal of $\sim 100 - 200$ p.e. while the rest of the camera remains dark. Since any external light source would result

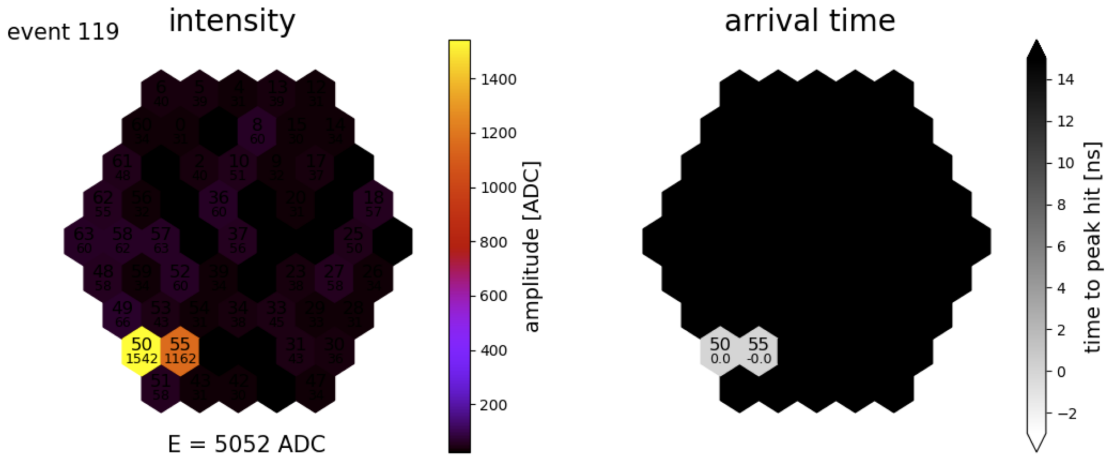

Figure 6.4: **Muon measurement.** Measurement in cooling box with a threshold of 15 p.e. and no coincidence. High, on two pixels confined signal with almost identical arrival times indicating a muon event.

in a more spread signal, the only explanation for the observed localization combined with the high intensities is Cherenkov light generated inside the Winston cones. This claim is supported by the arrival times of the signal, which indicate a trajectory of a very fast particle entering the cone of channel 55 and passing the one of channel 50 before leaving the camera. This matches the observation of a higher intensity of channel 50 well, since the path-length through this cone is expected to be longer and therefore more Cherenkov light is produced. By turning the camera upside down pointing towards the ground the signal vanished, which proofed that it gets shielded by the earth's mass - as expected for astrophysical muons.
Malfunction of the telescope and its electronics as origin for the signal could be ruled out beyond doubt, leading to the conclusion that the telescope, and the camera in particular, work well at temperatures down to -50^{o}C.

6.2 South Pole Measurement

In succession of the promising results in the Cool-Chamber, the IceACT telescope was deployed at the South Pole for a first real field test (Fig. 6.5).
Figure 6.6 shows the temperature development of the telescope. A power outage shut down the telescope. A cold start (Fig. 6.6 (a)) similar to the previous in the cooling chamber (Fig. 6.2) was successfully performed. The temperature of the TARGET module rises sharp until it gradually saturates $\sim 45^{o}$C above camera temperature. The fan remained switched off, which is the reason for the absence of the TARGET temperature drop (or rise of the camera temperature) as well as the temperatures of the box and the camera remaining low.

Figure 6.5: **IceACT Telescope at the South Pole.**

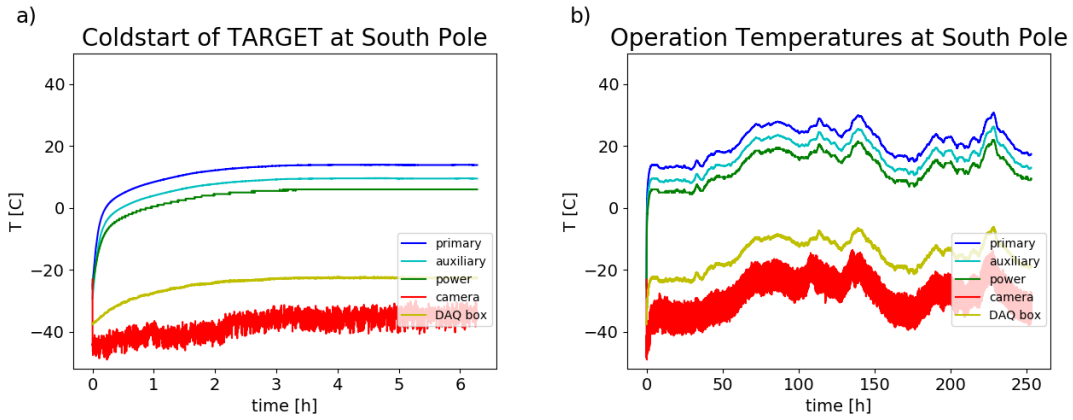

Figure 6.6: **Operational Temperatures at South Pole.** IceACT operated without fan. (a) Coldstart of TARGET after Power Outage until saturation is reached. (b) Operational Temperatures change with outside temperature and wind speeds, however, internal temperature gradient stays constant.

After reaching saturation, the temperature of the telescope changes with outside temperature and wind speed (Fig. 6.6 (b)). The internal temperature gradients, however, remain constant. It could be decreased by the use of the fan, however, it caused status quo no issues and provides the advantage of a cold, and therefore less noisy, camera.
Combined with the good shower images (section 7.1) one can conclude that the IceACT telescope worked well at the South Pole.

7 Air Showers

The IceACT telescope is designed to detect cosmic ray induced air showers. Measurements were taken next to ECAP in Erlangen and later reproduced at the H.E.S.S. observatory in Namibia as well as the South Pole.

7.1 Events

In Erlangen, triggering with a coincidence level $c_1 = 2$ allowed to set the threshold to ~ 15 p.e. With these settings, a rate of slightly more than 1 Hz was recorded, with a shower to noise ratio > 20. Since the showers are assumed to form a connected pattern in the camera, for later measurements in Namibia, as well as the South Pole, the requirement of neighbouring triggergroups exceeding the threshold was implemented. As a consequence of that and due to much less NSB and light pollution it was also possible to reduce the trigger threshold, resulting in a rate of ~ 8 events per second, however, the signal to noise ratio dropped to ~ 0.25.
A selection of faint to bright shower images is shown in Fig. 7.1. The displayed intensity is the peak-height of the Gaussian fit. By dividing by the gain the number of p.e. can be obtained. The filtering and the Gaussian fit allow for higher intensities than the saturation at ~ 3300 ADC counts (as discussed in chapter 3).
The intensity profile is in good agreement with the expected elliptical structure of the Cherenkov light produced in the showers (Fig. 1.5). The highest intensities are recorded in the center of the shower and decrease towards the outside.
The peak-time of the pixel with the highest intensity is taken as reference and shows the value of 0 in the peak-time plot. If either the intensity value is below 20 ADC counts (2.5 p.e.) or the time is not in the interval of -5 to 15 ns around the reference, the channel is assumed not to be hit by the shower. Since fitting on the noisy baseline can give values far beyond realistic numbers, these pixels are blacked for clearer representation.
The pixels with the highest intensities show the earliest peak-times, since their photons originate in the center of the shower and therefore have to travel slightly less distance to reach the camera. As the intensity decreases, the peak-time grows towards the outside, clearly showing, that both are correlated. The sampling time is 1 ns, however, by the filter and the Gaussian fit, the peak-time can be observed with sub ns precision.

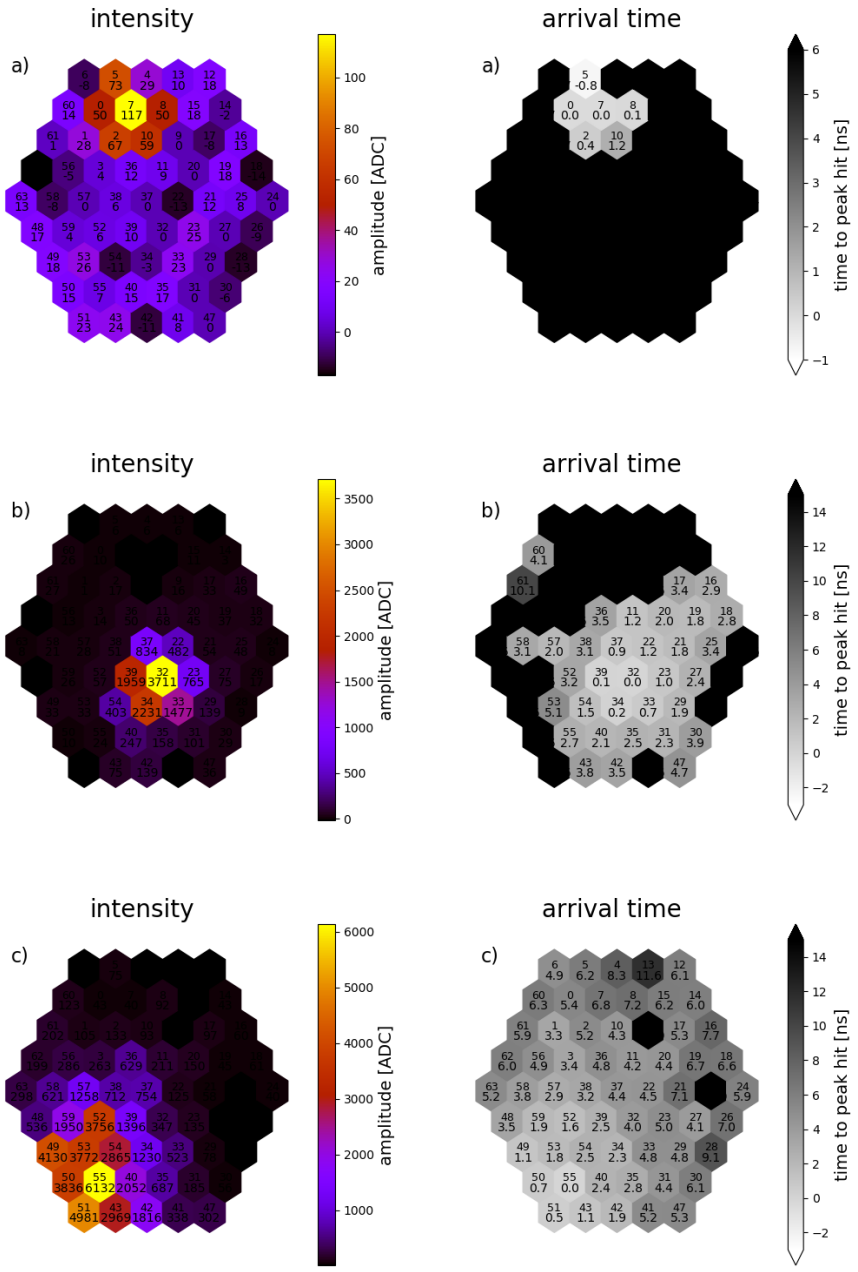

Figure 7.1: **Cosmic Ray air shower events.** Recorded events from the South Pole (a), Namibia (b) and Erlangen (c). The Peak-time is given relative to the arrival time of the channel with the highest intensity.

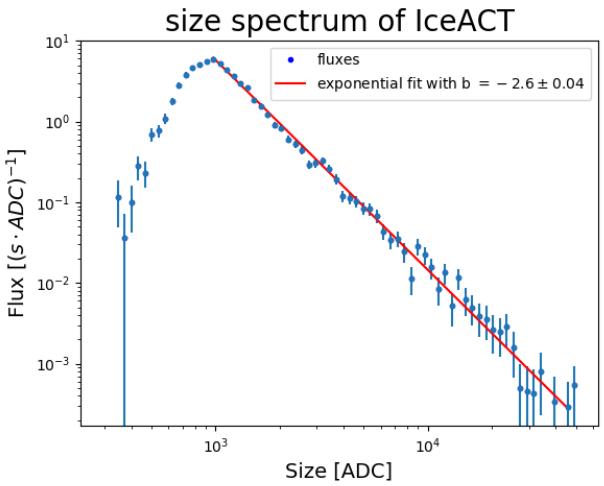

Figure 7.2: **Size spectrum of the Cosmic Rays detected with IceACT at Erlangen.** Above a threshold, the spectrum is well described by a power law with index -2.60 ± 0.04. This is slightly harder, than the expected -2.7 of the Cosmic Ray spectrum. Besides it remains questionable whether the index could be measured with sufficient precision, IceAct measures in the region below the cosmic "knee", where the index is indeed slightely smaller.

7.2 Size Spectrum

The energy of the incident particle can be reconstructed from the size and the impact point. This, however, requires simulations of the IceAct telescope, which were not available at the time of this thesis. Such, the best measure for the energy with this low level analysis is the total size of the IceAct events.
The sum of the intensities of all pixels is binned in logarithmic bins and divided by the bin range and is, for each bin, plotted at the logarithmic mean. Dividing this number by the measurement time, one obtains the count rate spectrum displayed in Fig. 7.2.
The maximum of the spectrum can be taken as the threshold. Below, the measured flux drops very fast, yet above it can be well fitted by a power law with an index of -2.60 ± 0.04. The cosmic ray spectrum (section 1.1) does follow a power law with index -2.7, however, the IceACT measures CRs in the regime below the "knee", where the index is slightly smaller. Such it matches the measurement - an extraordinary result considering the very low level of the analysis.

8 Energy Threshold

A good measure for the energy threshold - a property which is highly relevant for the IceCube veto application - is the maximum in the detected count spectrum. The energy of the incident particle can be reconstructed from the shower images, however, this requires simulations of the IceAct, which were not available at the time of the thesis. One other way to determine the energy is measuring in coincidence with a Cherenkov Telescope Array which can reconstruct the energy - for instance the H.E.S.S. observatory in Namibia. By matching the trigger time stamps, a H.E.S.S. events is associated with the right IceACT event, eventually resulting in a energy spectrum of IceAct.

8.1 Preparation and Measurement

The position of the IceACT telescope should be as close as possible to the center of the H.E.S.S. array to maximize coincident events. In the center, however, H.E.S.S. II is located, covering a large fraction of the sky due to its height of ~ 60 metres if one would set IceACT up close to it. To avoid this to still being able to observe the whole sky above the minimum altitude pointing angle of H.E.S.S. of 30^o, would require to move up to 85 m off the center of the array. This is already outside the array and therefore too far outside for convenient coincidence measurements. A solution was found by elevating the IceACT. The roof of the shelter of H.E.S.S. II proofed to be the best position and the exact set-up point is indicated by the red circle in Fig. 8.1.
To observe coincident events, it is required that IceACT and H.E.S.S. point in the same direction, which includes pointing and tracking. The IceACT is light enough to be mounted on a standard telescope mount, in this case the Skywatcher EQ8. With a 3-star alignment a pointing accuracy of $< 2^o$ was achieved. Since H.E.S.S. has a field of view of just 5^o this is sufficient to ensure that it is inside the 12.6^o field of view of IceACT and therefore no events are lost due to wrong pointing.
The H.E.S.S. site provides very good conditions to observe the sky, in particular, very low light pollution leads to very low background. The measurements were taken with an applied voltage to 28.4 V, referring to a gain of ~ 6 ADC. The trigger was also modified, as already mentioned in chapter 7. No longer a coincidence of any two triggergroups, but neighbouring ones is required to trigger. For low superpixel thresholds (single superpixel trigger-rate ~ 3000 Hz) this reduced the trigger rate by a factor ~ 3, while for high thresholds (single triggergroup rate ~ 300 Hz) it remained more or less constant. This indicates that indeed just noise events get cut and proofs the value of the modification especially for observations just above the threshold.

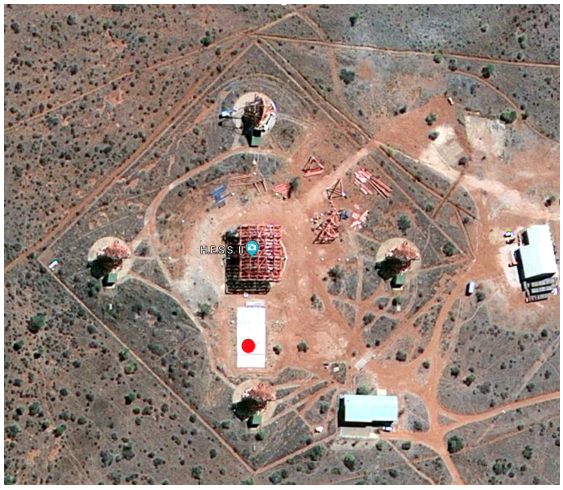

Figure 8.1: **Position of the IceACT in the HESS array.** The IceACT telescope was set up on the roof of the shelter of H.E.S.S. II. The position is indicated by the red circle.

8.2 Event correlation

Coincident measurements of roughly 28 hours were taken. Within that time, $\sim$ 908k DACT (IceACT was renamed DesertACT or DACT during the Namibia campaign) and $\sim$ 12.285k H.E.S.S. events were recorded and have to be matched. Latter are the remaining events after the analysis process ("zeta hybrid") including soft cuts on the size (CT1-4: 60 p.e.; CT5: 80 p.e.) and the local distance (CT1-4: 0.525 ; CT5: 0.72).

8.2.1 Time stamps

Differences in the data recording time, originating from such as breaks, calibration of the cameras or differing start and stop times, create events that can not be matched. Although their presence will have no impact on the energy spectrum obtained from the matching, it will affect quantitative calculations, in particular the percentage of matched events. After getting rid of these, 12.285.096 H.E.S.S. and 908.380 DACT events, detected in a measurement time of 103.091 s ($\sim 28,5$ h), remained.
The events were matched by comparing the time stamps. Each pair of DACT and H.E.S.S. event within a time window ($-j_{\max} < t < +j_{\max}$) is is considered a match, with the jitter being defined as the difference between the time stamps . The data sets were first matched with $j_{\max} = 0.7$ ms. The jitter distribution, as shown by the yellow curve in Fig. 8.2, revealed a double peak - a larger peak is followed by a smaller peak after $\sim$0.8 ms. Most likely, it originates from a jump of the CPU clock of the computer connected to the TARGET module.
One can correct for this effect by using the TACK time - the internal clock of the TARGET module. It starts counting at power on of the module and is by far more precise

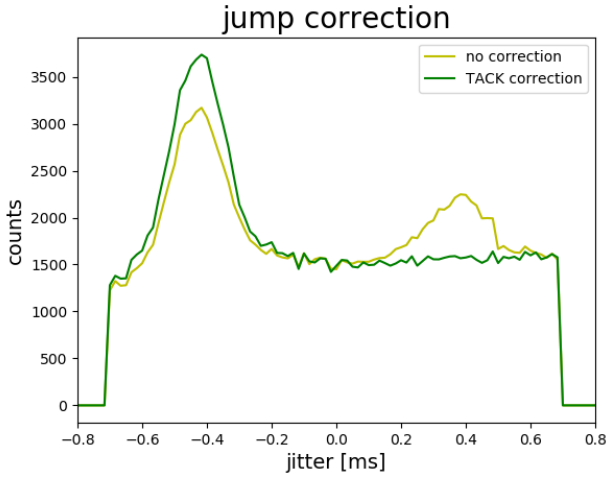

Figure 8.2: **Correction of 0.8 ms jump.** From matching the time stamps a double peak occurs due to a jump of the CPU clock of the readout computer. After correcting with the TACK time (internal clock of the TARGET module) just one peak remains. The whole jitter distribution is artificially shifted by 0.7 ms.

than the CPU clock. If the TACK time difference and the CPU time difference between two following events differs by more than 0.4 ms, the CPU time of the later one is corrected by this 0.8 ms. After correcting 27% of the events one obtains just one bigger peak (Fig. 8.2, green curve).
This jitter peak, however, is still not centred around 0 (Fig. 8.3 (left)). For all matches a constant shift of 0.27 ms is observed. A possible explanation being different electronic path lengths from the camera to the read out computers for H.E.S.S. and DACT. It can be corrected for by artificially shifting one series of timestamps by that value. As one obtains from Fig. 8.3 (a) the peak shape gets not affected by that process, which is just one evidence that the match pairs get not changed.
The matches consist of two components, real matches and random coincidences. They can be distinguished since the jitter of real matches is expected to be gaussian distributed, while the random matches create a constant offset. As a consequence, the number of matches over the $j_{\max}$ shows a linear dependency until the edge of the gaussian peak is reached (Fig. 8.3 (b)). The break of linearity was determined to 0.33 ms. It can be assumed, that for all larger values of $j_{\max}$ just noise but no more real events get matched, so that value was chosen as best $j_{\max}$.

8.2.2 First Match

$\sim$ 97k matches were found, with the best values for the shift of 0.27 ms and the $j_{\max} = 0.33$ ms (Fig. 8.4)). The mean intensity of the matched DACT events shows

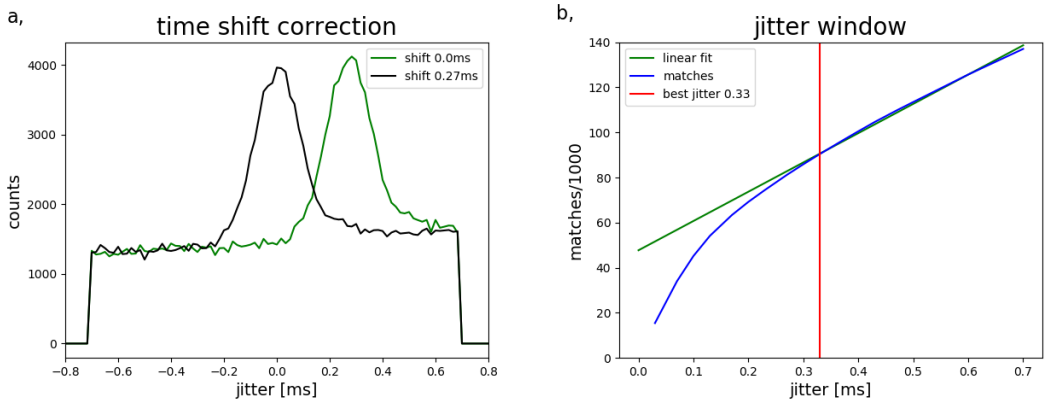

Figure 8.3: **Shift and jitter.** Due to different electronic paths a constant shift between the time stamps of DACT and H.E.S.S. occurs (left) and can be corrected for by an artificial offset (0.27 ms) to center the jitter peak around 0. The optimal jitter value is 0.33 ms, where the growth of matches with the rising time window becomes linear (right).

a bright circle of $\sim 5^o$ diameter (Fig. 8.4 (a)), which can be related to the H.E.S.S. field of view (fov). It is not centered in the DACT fov, despite the alignment of the mount was achieved with below 1^o precision, since the aligning pointer was not parallel to the DACT telescope. The deviation, however, is small enough so it can be assumed that the entire H.E.S.S. fov was observed by the DACT. The fact, that it just emerges after the matching proofs - supported by the tendency to a linear dependency of the DACT/H.E.S.S. size (Fig. 8.4 (d)) and the gaussian peak in the jitter distribution - that real matches are found.
Despite observing a gaussian peak, the jitter distribution shows a very large offset, indicating that the matches are still dominated by random coincidences. For low energies they dominate the count spectrum, which is the reason why no peak can be observed in the matched energy spectrum (Fig. 8.4 (e)).
Both, the number of expected real and random matches can be calculated quantitatively. The rate of noise trigger of DACT

$$r_{\mathrm{D,n}} = r_{\mathrm{SP}}^2 \cdot \Delta t_{\mathrm{trig}} \cdot N_{\mathrm{neigh}} = 5.40\mathrm{Hz} \tag{8.1}$$

can be calculated from the threshold rate of a single superpixel $r_{SP} = 3\mathrm{kHz}$, the trigger window $\Delta t_{\mathrm{trig}} = 20ns$ and the number of neighbouring pairs of superpixels $N_{\mathrm{neigh}} = 30$ (superpixel 12 was excluded due to malfunction). As the total DACT rate is 7.24 Hz, 1.84 Hz events remain.
H.E.S.S. is 1000 times more sensitive than DACT, however, still not all events DACT observed were also detected by H.E.S.S. due to its smaller field of view. Under the assumption, that the DACT events are homogeneously distributed, applying a geometry factor

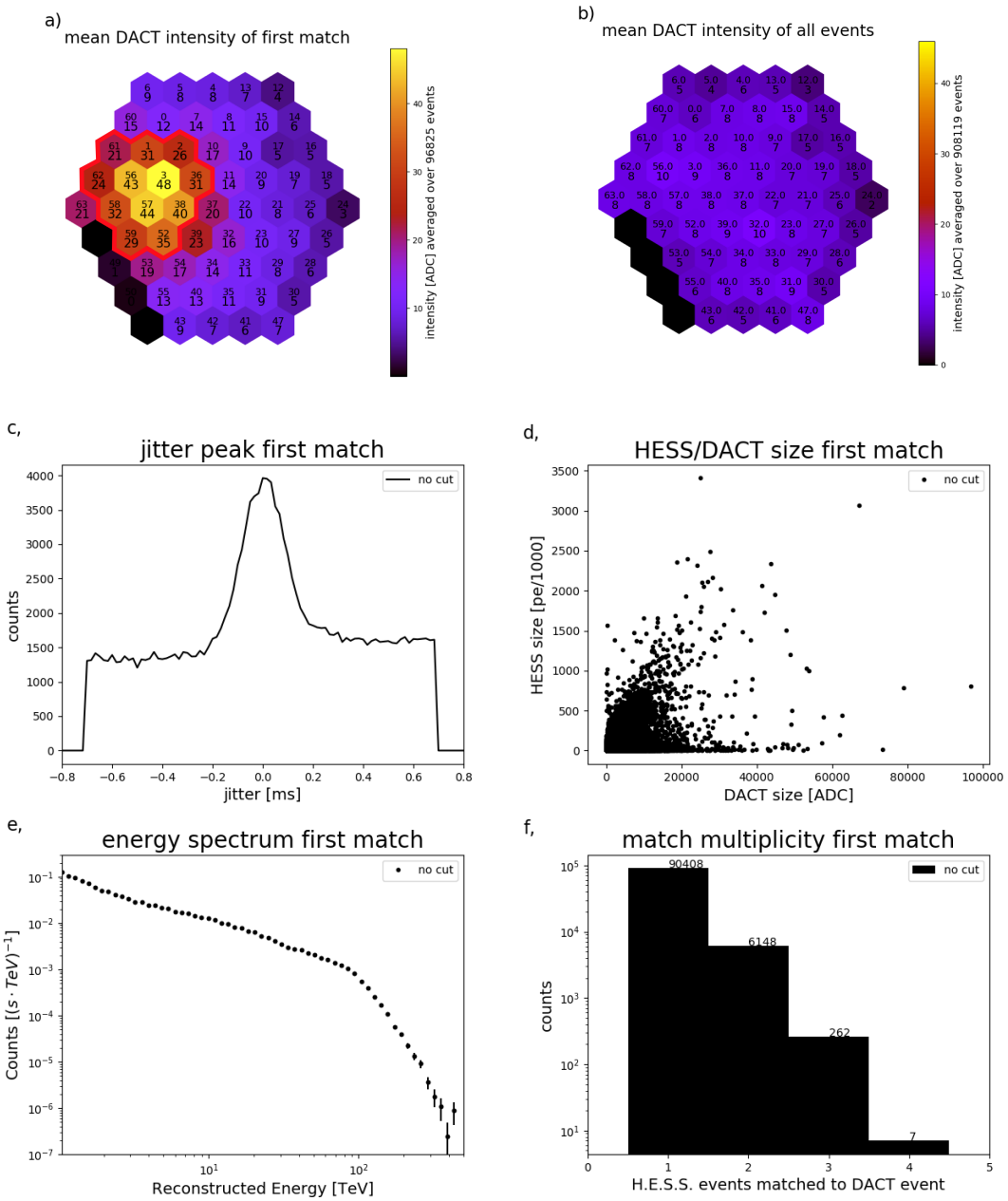

Figure 8.4: **Events matched without applying pre-cuts.** The H.E.S.S. fov (red enclosure) can be seen in the mean intensity of the DACT pixels of the matched events (a), while absent in the mean intensity of all events (b). The jitter distribution of the matches (c) shows a gaussian peak, however, the large offset is due to many wrong matches which are randomly distributed. According to c, the H.E.S.S. over DACT size (d) shows a correlation, but again a lot of random distributed points referring to the large percentage of noise in the matches. This is the reason, why no peak can be obtained in the energy spectrum of the matches (e). The total number of matches (sum of the values in f) of ∼97k is reasonably close to the predicted number of ∼89k.

$$f_{\text{fov}} = \frac{A_{\text{fov,H}}}{A_{\text{fov,D}}} = 0.16 \tag{8.2}$$

gives the rate of matchable events

$$r_{\text{D,ev}} = (r_{\text{D}} - r_{\text{D,n}}) \cdot f_{\text{fov}} = 0.29\text{Hz} \tag{8.3}$$

and successively the total number of matchable events

$$N_{\text{real}} = r_{\text{D,ev}} \cdot t_{\text{meas}} = 29896. \tag{8.4}$$

Note that in this calculation the expansion of the shower is neglected and therefore the total number of real matches slightly underestimated.
Random matches arise from random coincidence of the timestamps. Their total number

$$N_{\text{random}} = r_{\text{D}} \cdot r_{\text{H}} \cdot 2j_{\text{max}} \cdot t_{\text{meas}} = 56367. \tag{8.5}$$

depends linearly on the rates of H.E.S.S. $r_{\text{H}} = 119.2$ Hz and DACT $r_{\text{D}} = 7.25$ Hz, as well as the jitter window and the measurement time. Real and wrong matches add up to $\sim$ 89k, which is reasonably close to the $\sim$97k matches, that are actually found, considering the simplifications and assumptions taken.

8.2.3 Precuts

To obtain a peak in the count spectrum the number of random matches has to be reduced, which can be achieved by reducing the rates of H.E.S.S. and DACT (equation 8.5). One possibility is to apply pre-cuts to the H.E.S.S. or DACT data, however, they should be chosen as soft as possible to avoid cutting real matches.
The threshold of DACT was chosen very low, so no possible detectable events are lost due to the trigger. As a consequence, a lot of noise is triggered as well. An effective way to cut it is time delta cleaning. It tests the arrival time and position on the camera of the brightest and the next brightest pixel. For shower events, both are expected to be close, while for noise events they can be randomly distributed. In this case, an event is assumed a shower if the brightest and the next brightest pixel are at least next neighbours and their peak times differ by less than a time window t_{w}.
On top, the H.E.S.S. fov was seen in the matched events (Fig. 8.4 (a), red enclosure). Due to that, the requirement, that one of the two brightest pixels lies within the H.E.S.S. field of view, was added. Additionally, If the sum of the intensities of all pixels within the H.E.S.S. fov exceeds a threshold an event is kept, independent of the other criteria. This is to ensure that very bright showers, centred outside this field of view but still bright enough in it, do not get cut.
The results of the cuts on the DACT data for different t_{w} are shown in Fig. 8.5. A time window $t_(w) = 8$ns was chosen, since among all time windows it has the best ratio of peak-height to offset in the jitter distribution (Fig. 8.5 (c)), indicating the best real to random match ratio. The energy spectrum of the matches (Fig. 8.5 (b)) shows that

a,

t_w[ns]	ev.	r [Hz]	mat.	pred.
20.0	188k	1.82	44k	45k
10.0	179k	1.74	43k	44k
8.0	170k	1.64	42k	43k
4.0	135k	1.31	37k	40k
2.0	102k	0.99	29k	38k
0.7	55k	0.53	15k	34k

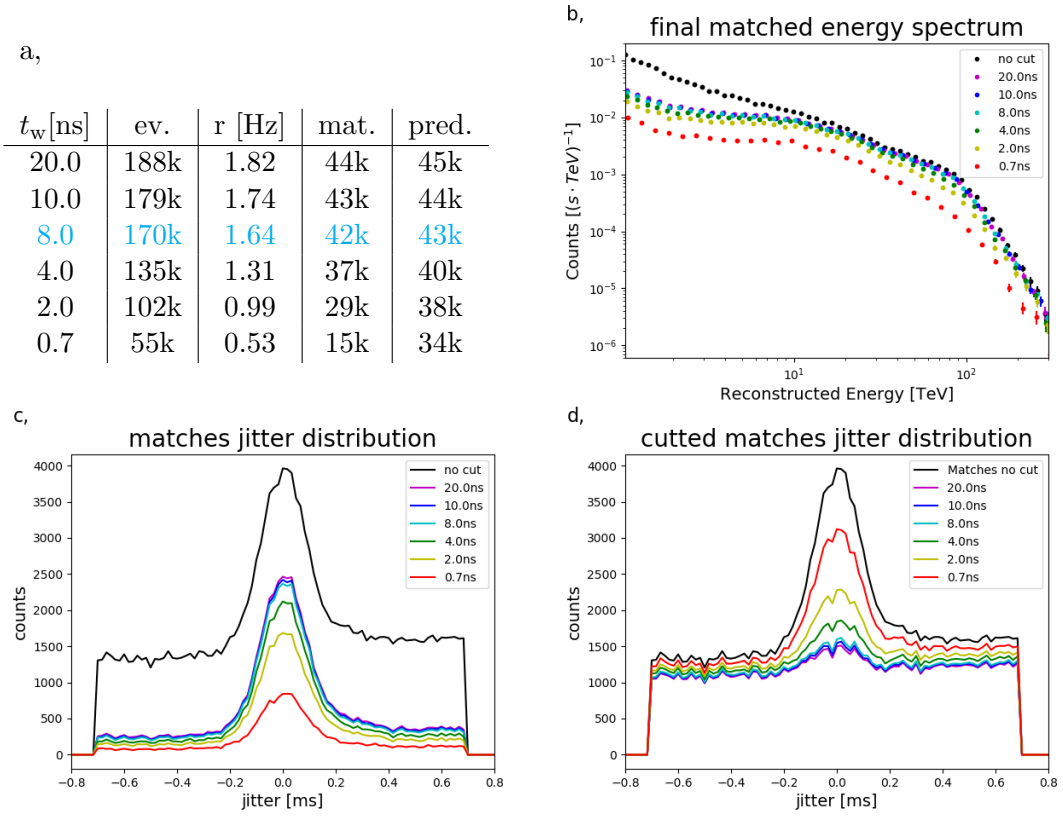

Figure 8.5: **Time delta cleaning and field of view cut on DACT data.** Remaining events/rate (a), energy spectrum of the remaining matched events (b) and jitter distribution of the kept (c) and cut (d) events for different time windows t_w. A time window of 8 ns was chosen, since the peak in the cutted matches saturates at a minimum and still a large part of the random offset gets cut. Additionally, the ratio of peak-height to offset in the matches jitter distribution is high and from the energy spectrum one can obtain that for high energies almost no events get cut. Further, the amount of predicted and observed matches fits well, which also indicates that almost all real matches are kept.

just low energetic events are cut, while for smaller time windows the rate drops for all energies. The jitter distribution of the cut matches (Fig. 8.5 (d)), however, shows even for high large windows a small peak, which shows, that real events get cut. The peak area - a measure for their amount - is closely related to the difference of predicted and observed matches (Fig. 8.5 (a)). For $t_w = 8$ns, the peak saturates in a minimum, as well as the prediction and observation of the number of matches are in good agreement.This supports the claim, that a time window of 8ns is the best choice.
As the measurement was taken down and below the threshold, it is impossible to separate noise from signal entirely. The time cleaning, however, showed a very good signal to noise ratio by reducing the total number of matches from 97k to 42k, while presumingly just $\sim$ 1000 real matches are lost. From the new DACT rate of $\sim$ 1.64Hz, the prediction of the random matches drops to 13k. Substracting these from the $\sim$ 42k found matches, leaves 29k real matches - very well fitting the predicted number and strongly supporting the claim, that the time delta cleaning with $t_w = 8$ns leaves the real matches mostly untouched.
As a consequence, the percentage of noise dropped from $\sim$70% to $\sim$32%. This, however, is still too much to observe a peak in the matched energy spectrum (Fig. 8.5 (b)).
One possibility to further decrease the amount of random matches is cutting the enormous H.E.S.S. rate. This would be highly effective , however, it was not possible to find criteria, that do not cut real matches. The impact point is not reconstructed with sufficient precision and size cuts delete predominately events with smaller energy. This changes the spectrum, in particular the position of the threshold, and therefore size cuts are no option either.

8.2.4 Matched energy spectrum

An alternative way to get the random matches out of the energy spectrum is to determine the energy spectrum of pure random matches and subtract it. The best way to create such a spectrum is by matching the real data with a large shift compared to the chosen j_{max} of 0.33 ms.
The results from such a match with a shift of 100 ms can be obtained in Fig. 8.6. The jitter distribution (Fig. 8.6 (a)) shows the constant offset, but as expected, the gaussian peak vanishes. The total number of random matches is $\sim$ 13k, which very well matches the prediction from the previous section. Additionally, the offsets of the random and real match are more or less the same, indicating, that in both cases the amount of random matches is the same.
The energy spectrum of the random matches (Fig. 8.6 (b)) shows a power law with the same index of the original H.E.S.S. spectrum at just a lower amplitude. Even spectral features, like the dip at $\sim$ 100 TeV followed by a faster decrease - an artefact of the energy reconstruction of H.E.S.S. - can be observed. This is in perfect agreement with the expectation of a spectrum of random chosen events.
Both together, the amount and the spectrum of the random matches, allow for the conclusion, that the energy distribution of the match with shift 100 ms is the same as of the

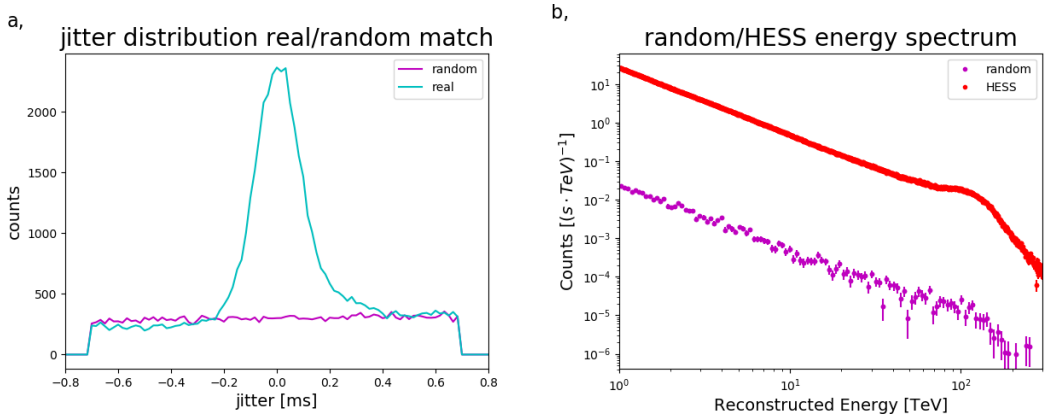

Figure 8.6: **Random Match.** The jitter distribution (a) and energy spectrum of the remaining events compared to the total H.E.S.S. energy spectrum (b) for a match with shift 100 ms and the applied time delta cleaning ($t_w = 8$ns). The peak in the jitter distribution vanishes, with just the constant offset due to the random matches remaining. The spectrum matches the power law of the original H.E.S.S. spectrum. Both together allow for the assumption, that this match is indeed similar to the spectrum of the random matches for a shift of 0.27 ms.

random matches within the match with 0.27 ms. As a consequence, the energy spectrum of the random matches can be used as a correction of the previously obtained matched energy spectrum.
The final matched energy spectrum of DACT is shown in Fig. 8.7. Now, indeed a peak can be observed.

8.3 Threshold

8.3.1 Calculation

The spectrum, including the exponential cut-off below the threshold, can be well described by a smoothly broken power law

$$f(E) = a \cdot E^{b_1} \left[1 + \left(\frac{E}{E_t} \right)^{\frac{b_2 - b_1}{\gamma}} \right]^{-\gamma} \tag{8.6}$$

which features two power laws with indexes $b_{1/2}$ and a smooth transition between both at E_t.
The energy at the maximum of f, defined as the threshold, can be determined from an equation where the first derivative

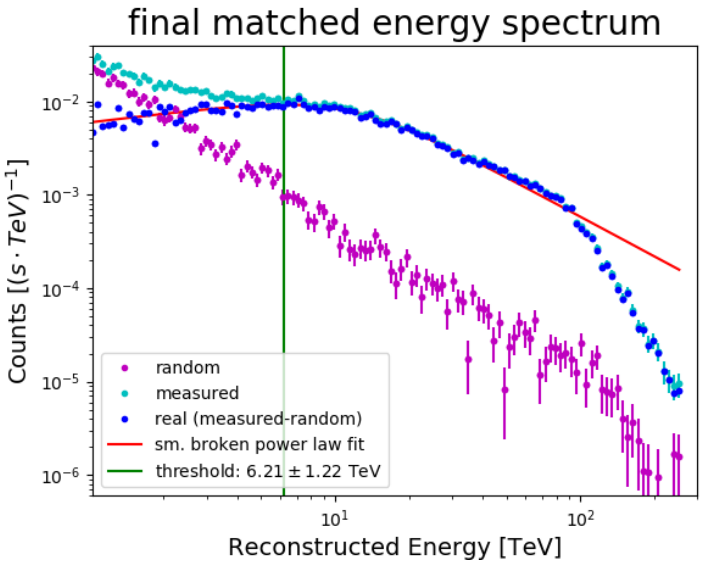

Figure 8.7: **Energy threshold of IceACT.** Random matched energy spectrum (magenta) is subtracted from the measured matched energy spectrum (cyan) to obtain the final (real) matched energy spectrum (blue). Latter is fitted with a smoothly broken power law (red), with its peak being the energy threshold of IceACT (green).

$$\frac{\mathrm{d}f}{\mathrm{d}E} = -ab_1 \left[E^{-b_1-1}\right] \left[1 + \left(\frac{E}{E_t}\right)^{\frac{b_2-b_1}{\gamma}}\right]^{-\gamma-1} \left[1 + \frac{b_2}{b_1} E_t^{\frac{b_1-b_2}{\gamma}} E^{\frac{b_2-b_1}{\gamma}}\right] \stackrel{!}{=} 0 \tag{8.7}$$

is set equal to 0 (calculation of the derivative in Appendix 10.1.1). The first factor only gives 0 for the non-physical case of $E = 0$. The second term gives (for most cases) no solution (Appendix 10.1.2) and for the few exceptions it is negative and therefore again non-physical. From the third term, however, one can obtain the value of the threshold (Appendix 10.1.3)

$$E_{\mathrm{thresh}} = \left(-\frac{b_1}{b_2}\right)^{\frac{\gamma}{b_2-b_1}} \cdot E_t \tag{8.8}$$

For physical cases $b_1 > 0$ and $b_2 < 0$, which is the reason why this equation is solvable and the extrema is a maximum.
The total error on the threshold

$$\Delta E_{\mathrm{thresh}} = \frac{\partial E_{\mathrm{thresh}}}{\partial b_1}\Delta b_1 + \frac{\partial E_{\mathrm{thresh}}}{\partial b_2}\Delta b_2 + \frac{\partial E_{\mathrm{thresh}}}{\partial E_t}\Delta E_t + \frac{\partial E_{\mathrm{thresh}}}{\partial \gamma}\Delta\gamma \tag{8.9}$$

can be determined by an error propagation. It is the sum of the partial derivative multiplied with the error of each fit parameter.

8.3.2 Fit

The fit of the smoothly broken power law to the final matched energy spectrum is shown by the red curve in Fig. 8.7. Despite the region above the softening, which is irrelevant for the determination of the threshold, the fit matches the spectrum well. As a result, the energy threshold could be determined to 6.21 ± 1.22 TeV.
Important to mention is, that the reconstruction of the energy of the H.E.S.S. events is based on gamma like events, so it effectively measures the energy of the electromagnetic sub-showers within the hadronic shower. One can perform simulations with the application of the same cuts as in the real analysis, to determine the most likely true proton energy related to a reconstructed gamma energy of ~ 6.21 TeV.
Fig. 8.8 (left) shows the the reconstructed gamma energy depending on the true proton energy fed to the simulation. The distribution of the true proton energies of showers with reconstructed energies around the measured threshold of $6.00 - 6.25$ TeV (Fig. 8.8 (right)) shows a clear peak. Its position is the superior value for the true proton energy of the threshold compared to the mean of the whole distribution, since many showers with impact points far away of the camera appear dark and therefore are reconstructed with far too low energies. As a consequence, a lot of high energy showers contribute to the mean of the simulation, however, in reality they would be too dark to be observed by IceAct.
The position of the peak is determined with a Gaussian fit. For the same reason of the

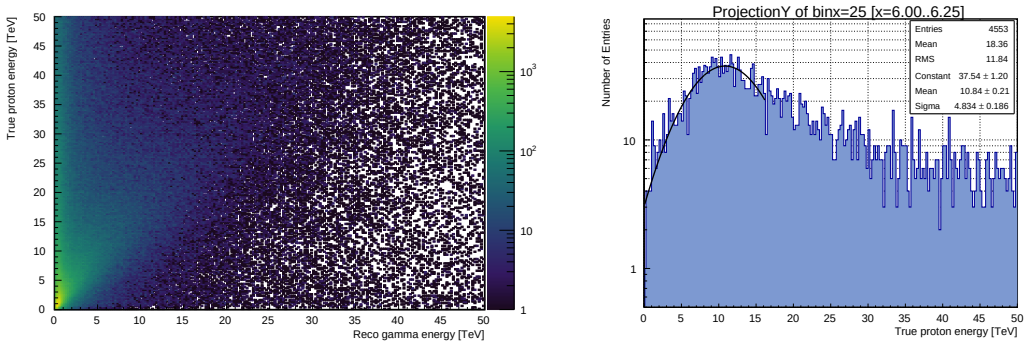

Figure 8.8: **True proton energy of the threshold.** True proton energy over reconstructed electromagnetic energy for energies up to 50 TeV (left) and vertical profile for the bin between 6.00 and 6.25 TeV (right). The most likely true proton energy of the threshold can be determined by the position of the maximum of a Gaussian fit. It gives a true proton energy of $\sim$ 11TeV.

wrong contribution of outlying showers, the fit range is restricted to the lower energy part of the distribution. With that, the most likely true proton energy of the energy threshold of IceAct was determined to $\sim$ 11 TeV. This shows improvement compared to a threshold of $\sim$ 20 TeV of an earlier IceAct design, however, it is important to mention, that especially the determination of the real proton energy underlies great uncertainties. [11]

9 Summary and Outlook

The IceACT is a small scale Cherenkov telescope, based on the conceptual idea of large arrays. A large field of view of $\sim 12.6°$, low total cost per telescope < 10k€ and low power consumption ~ 36W make it suitable for that.
This thesis reports the set-up, calibration and testing of the Erlangen design of an IceAct telescope.
The hard-shell of the telescope is based on the design from RWTH Aachen, however, some changes were applied. The fiber glass tube was replaced by a much lighter plastic version - lowering the total weight such, that the whole IceACT could be mounted on a standard telescope mount. The data acquisition box, with one major change by including the TARGET C readout electronics as its heart, was attached to the bottom of the tube, right below the camera. By that, the telescope got more compact and therefore much more resilient to environmental influences. This could be proven by successful operating the IceACT, including a cold start of the whole electronics, first in a cool chamber down to -50°C and later during the polar night at the South Pole.
New fabrication methods of the Winston Cones improved their homogeneity significantly. The remaining deviations, as well as internal deviations of the properties of the SiPMs, could be calibrated by illumination with homogeneous laser radiation. After the calibratio the intensity deviated by less than 5% for the vast majority of pixels, while deviations of the arrival time were on the order of ~ 0.2ns. Additionally, an internal regulation of the gain was developed. It uses dark counts present in the detected waveforms before the data peak to determine the present gain. Deviations to a set value are corrected by the applied voltage. This was only possible for the mean value of a whole trigger group with this TARGET module, but will be possible for each pixel individually in the upcoming version.
A field test at Erlangen showed clear shower images. Its Size spectrum well followed a power law with index ~ 2.6 above the threshold, strongly indicating that indeed Cosmic Ray events were detected.
The energy threshold of this design of IceACT was determined by measuring in coincidence with the H.E.S.S. array in Namibia. Due to the absence of a shower property reconstruction for IceACT - one of the most urgent future tasks - matching the triggered timestamps of IceACT with H.E.S.S. was the only possibility to determine the energy of the detected IceACT events. With that method, the energy threshold of IceACT could be determined to ~ 11TeV - showing good improvement to an earlier design with a threshold of ~ 20 TeV.
The results in this thesis showed, that the IceACT in principle works at the South Pole, the location of its main and naming application - a large array above IceCube to veto terrestrial neutrinos. The dependency on dark time, however, make it questionable

whether it will be an improvement compared to the existing IceTop array. None the less, the location of the South Pole provides very good conditions for observations of showers with energies around the "cosmic knee" ($\sim 10^{15}$TeV). It is predicted, that a reconstruction based on the images of an array of just 7 telescopes - a much more realistic goal at least on short term - will be sufficient to determine the incident particle species. With that, one wants to perform composition studies in that energy range to shed light on the processes that accelerate particles within and outside our galaxy.

Bibliography

[1] Cherenkov telescope array - exploring the universe at the highest energies. https://www.cta-observatory.org.

[2] *Datasheet - SensL MicroFJ-60035-TSV.*

[3] Hess. https://www.mpi-hd.mpg.de/hfm/HESS/.

[4] The magic telescopes. https://magic.mpp.mpg.de.

[5] *Product Information Sheet - EPOTEK 310M-2.*

[6] C. Amsler. Cosmic rays. *Physical Letters*, B667(1), 2008.

[7] J Auffenberg, Thomas Bretz, Lukas Middendorf, Tim Niggemann, Leif Rädel, Merlin Schaufel, Sebastian Schoenen, Johannes Schumacher, and Christopher Wiebusch. Design study of an air-cherenkov telescope for harsh environments with efficient air-shower detection at 100 tev. *researchgate*, 2015.

[8] Jan Auffenberg. Iceact: Imaging air cherenkov telescopes with sipms at the south pole for icecube-gen2, 2017.

[9] Konrad Bernlöhr. Atmospheric cherenkov light. https://www.mpi-hd.mpg.de/hfm/CosmicRay/ChLight/Cherenkov.gif. visited at 02.10.2018.

[10] D. J. Bird. Evidence for correlated changes in the spectrum and composition of cosmic rays at extremely high energies. *Physical Review Letters*, 71(3401), 1993.

[11] Thomas Bretz. Extending wide fov gamma-ray observations with an array of compact cherenkov telescope, May 2019.

[12] IceCube collaboration. Cosmic rays. https://icecube.wisc.edu/ tmontaruli/801/lect14.pdf. visited at 25.09.2018.

[13] Daniele Dallacasa. Radiative processes and mhd. *http* : *//www.ira.inaf.it/ ddallaca/Cosmic*$_r$*ays.pdf*, 2016. visited at 01.10.2018.

[14] Deutscher Wetter Dienst. Icao standardatmosphäre. https://www.dwd.de/DE/service/lexikon/begriffe/S/Standardatmosphaerepdf.pdf. visited at 01.10.2018.

[15] Personal discussion with Jan Auffenberg (RWTH Aachen).

[16] Personal discussion with Merlin Schaufel (RWTH Aachen).

[17] THE EDITORS. The world's oldest writing. *Archeology*, 2018.

[18] Ray Davies et. al. A search for neutrinos from the sun. *Physical Review Letters*, 20(21):1205–1209, 1968.

[19] M. Frank and I. Tamm. Coherent visible radiation of fast electrons passing through matter. *Comptes Rendus (Doklady) de l'Académie des Sciences de l'URSS, Nouvelle Série*, 14, 1936.

[20] S. Funk, D. Jankowsky, H. Katagiri, M. Kraus, A. Okumura, H. Schoorlemmer, A. Shigenaka, H. Tajima, L. Tibaldo, G. Varner, A. Zink, J. Zorn, and for the CTA Consortium. Target: A digitizing and trigger asic for the cherenkov telescope array. 2016.

[21] Karlsruhe Institut für Technologie (KIT). Galactic knee and galactic ankle, 2017.

[22] W. Heitler. *The Quantum Theory of Radiation.* Oxford University Press, 3rd edition, 1954.

[23] B. Herrmann. Development and characterization of a test stand for compact high energy camera (chec-s) mass test. Master's thesis, FAU Erlangen-Nuremburg, 2018.

[24] V. F. Hess. Über beobachtungen der durchdringenden strahlung bei sieben freiballonfahrten. *Physikalische Zeitschrift*, 13:1084–1091, 1912.

[25] Erwin Hubble. A relation between distance and radial velocity among extra-galactic nebulae. *Proceedings of the National Academy of Sciences*, 15(3), March 1929.

[26] IPFS. Cherenkov radiation. https://ipfs.io/ipfs/QmXoypizjW3WknFiJnKLwHCnL72vedxjQkDDP1m visited at 02.10.2018.

[27] Alexander Kobzev. The mechanism of vavilov-cherenkov radiation. *Physics of Particles and Nuclei*, 41:452–470, 2010.

[28] Jan Paul Koschinsky. Development of a 61-pixel camera for the iceact imaging air cherenkov telescope. Master's thesis, Rheinisch-Westfäische Technische Hochschule Aachen, 2017.

[29] K. Kremer. Development and testing of an iceact imaging atmospheric cherenkov telescope with target c based electronics. Master's thesis, FAU Erlangen-Nuremberg, 2018.

[30] A. Marshack. The roots of civilization: The cognitive beginnings of man's first art, symbol and notation. *New York: Moyer Bell*, 1991.

[31] J. Matthews. A heitler model of extensive air showers. *science direct*, 2004.

[32] T. Niggemann. The optics and detector simulation of the air fluorescence telescope famous for the detection of cosmic rays. *SPIE Astronomical Telescopes+Instrumentation*, 2012.

[33] T. Niggemann, P. Assis, P. Brogueira, A. Bueno, H. M. Eichler, M. Ferreira, T. Hebbeker, M. Lauscher, L. Mendes, L. Middendorf, S. Navas, C. Peters, M. Pimenta, A. Ruiz, J. Schumacher, and M. Stephan. Status of the silicon photomultiplier telescope famous for the fluorescence detection of uhecrs. 2015.

[34] Martin Schroedter. Particle showers produced in earths atmosphere. https://veritas.sao.arizona.edu/. visited 26.09.2018.

[35] J. Schäfer. Parameter optimization of the t5tea-asic for the cherenkov telescope array. Master's thesis, FAU Erlangen-Nürnberg, 2016.

[36] L. Tibaldo, J. A. Vandenbroucke, A. M. Albert, S. Funk, T. Kawashima, M. Kraus, A. Okumura, L. Sapozhnikov, H. Tajima, G. S. Varner, T. Wu, A. Zink, and for the CTA consortium. Target: toword a solution for the readout electronics of the cherenkov telescope. 2015.

[37] Arno Penzias; Robert W. Wilson. A measurement of excess antenna temperature at 4080 mc/s. *Astrophysical Journal Letters*, 142, 1965.

[38] N. Wolchover. The particle that broke a cosmic speed limit. *Quanta Magazine*, 2015.

10 Appendix

10.1 Smoothly broken power law

10.1.1 Derivative of smoothely broken power law

$$\frac{\mathrm{d}}{\mathrm{d}E}\left(a\cdot E^{-b_1}\left[1+\left(\frac{E}{E_t}\right)^{\frac{b_2-b_1}{\gamma}}\right]^{-\gamma}\right)= \tag{10.1}$$

$$=a\cdot\left\{-b_1E^{-b_1-1}\left[1+\left(\frac{E}{E_t}\right)^{\frac{b_2-b_1}{\gamma}}\right]^{-\gamma}-\gamma\left[1+\left(\frac{E}{E_t}\right)^{\frac{b_2-b_1}{\gamma}}\right]^{-\gamma-1}\cdot\frac{b_2-b_1}{\gamma}\left(\frac{E}{E_t}\right)^{\frac{b_2-b_1}{\gamma}-1}\cdot\frac{1}{E_t}\cdot E^{-b_1}\right\}= \tag{10.2}$$

$$=-ab_1\cdot\left\{E^{-b_1-1}\left[1+\left(\frac{E}{E_t}\right)^{\frac{b_2-b_1}{\gamma}}\right]^{-\gamma}+\left[1+\left(\frac{E}{E_t}\right)^{\frac{b_2-b_1}{\gamma}}\right]^{-\gamma-1}\cdot\left(\frac{b_2}{b_1}-1\right)\left(\frac{E}{E_t}\right)^{\frac{b_2-b_1}{\gamma}-1}\cdot\frac{1}{E_t}\cdot E^{-b_1}\right\}= \tag{10.3}$$

$$=-ab_1\cdot\left\{E^{-b_1-1}\right\}\left\{\left[1+\left(\frac{E}{E_t}\right)^{\frac{b_2-b_1}{\gamma}}\right]^{-\gamma-1}\right\}\left\{1+\left(\frac{E}{E_t}\right)^{\frac{b_2-b_1}{\gamma}}+\left(\frac{b_2}{b_1}-1\right)\left(\frac{E}{E_t}\right)^{\frac{b_2-b_1}{\gamma}-1}\cdot\frac{1}{E_t}\cdot E\right\}= \tag{10.4}$$

$$=-ab_1\cdot\left\{E^{-b_1-1}\right\}\left\{\left[1+\left(\frac{E}{E_t}\right)^{\frac{b_2-b_1}{\gamma}}\right]^{-\gamma-1}\right\}\left\{1+E_t^{-\frac{b_2-b_1}{\gamma}}E^{\frac{b_2-b_1}{\gamma}}+\left(\frac{b_2}{b_1}-1\right)E_t^{-\left(\frac{b_2-b_1}{\gamma}-1\right)-1}E^{\frac{b_2-b_1}{\gamma}}\right\}= \tag{10.5}$$

$$=-ab_1\cdot\left\{E^{-b_1-1}\right\}\left\{\left[1+\left(\frac{E}{E_t}\right)^{\frac{b_2-b_1}{\gamma}}\right]^{-\gamma-1}\right\}\left\{1+\left(1+\frac{b_2}{b_1}-1\right)E_t^{-\left(\frac{b_2-b_1}{\gamma}\right)}E^{\frac{b_2-b_1}{\gamma}}\right\}= \tag{10.6}$$

$$=-ab_1\cdot\left\{E^{-b_1-1}\right\}\left\{\left[1+\left(\frac{E}{E_t}\right)^{\frac{b_2-b_1}{\gamma}}\right]^{-\gamma-1}\right\}\left\{1+\frac{b_2}{b_1}E_t^{-\left(\frac{b_2-b_1}{\gamma}\right)}E^{\frac{b_2-b_1}{\gamma}}\right\} \tag{10.7}$$

10.1.2 2. Term of the derivative

$$\left[1+\left(\frac{E_{\mathrm{thresh}}}{E_t}\right)^{\frac{b_2-b_1}{\gamma}}\right]^{-\gamma-1}\stackrel{!}{=}0 \tag{10.8}$$

$$1 + \left(\frac{E_{\text{thresh}}}{E_t}\right)^{\frac{b_2-b_1}{\gamma}} = 0 \tag{10.9}$$

$$\left(\frac{E_{\text{thresh}}}{E_t}\right)^{\frac{b_2-b_1}{\gamma}} = -1 \tag{10.10}$$

$$\frac{E_{\text{thresh}}}{E_t} = (-1)^{\frac{\gamma}{b_2-b_1}} \tag{10.11}$$

Right side not solvable except for very special parameters!

10.1.3 3. Term of the derivative

$$1 + \frac{b_2}{b_1} E_t^{-\left(\frac{b_2-b_1}{\gamma}\right)} E_{\text{thresh}}^{\frac{b_2-b_1}{\gamma}} \stackrel{!}{=} 0 \tag{10.12}$$

$$\frac{b_2}{b_1} E_t^{-\left(\frac{b_2-b_1}{\gamma}\right)} E_{\text{thresh}}^{\frac{b_2-b_1}{\gamma}} = -1 \tag{10.13}$$

$$E_{\text{thresh}}^{\frac{b_2-b_1}{\gamma}} = -\frac{b_1}{b_2} E_t^{\left(\frac{b_2-b_1}{\gamma}\right)} \tag{10.14}$$

$$E_{\text{thresh}} = \left(-\frac{b_1}{b_2}\right)^{\frac{\gamma}{b_2-b_1}} E_t \tag{10.15}$$

For physical cases $b_1 >$ and $b_2 < 0$ are valid. By that $-\frac{b_1}{b_2}$ becomes positive and the equation is solvable.

Acknowledgments

I would like to thank everyone, who contributed or assisted me during the process of writing this Master's thesis. In particular

- Prof. Dr. Stefan Funk not just for the interesting (and at times challenging) topic, but also the great opportunity of performing measurements in Namibia

- Dr. Adrian Zink for any sort of help and advice, no matter the time of the day

- Dr. Lenka Tomankova for the dedicated contribution to the measurements in Namibia, which would not have been possible without

- Johannes Schäfer for many hours of productive work as well as good conversations

- David Jankowsky for his contribution of simulations, despite it was far off his own topic

- all the members at ECAP - cleaning stuff, technicians as well as colleagues - for all the nice smiles and a really outstanding work atmosphere!

Eigenständigkeitserklärung

Ich versichere hiermit, die Masterarbeit ohne fremde Hilfe und ohne Benutzung anderer, als der angegebenen Quellen angefertigt zu haben und dass die Arbeit in gleicher oder ähnlicher Form noch keiner anderen Prüfungsbehörde vorgelegen hat. Alle Ausführungen der Arbeit, die wörtlich oder sinngemäß übernommen wurden, sind als solche gekennzeichnet.

Erlangen, den